

POLITECNICO DI MILANO

Facoltà di Ingegneria Industriale

Corso di Laurea in Ingegneria Meccanica



Algorithms for infrared image processing

Relatore: Prof. Marcello Vanali, Politecnico di Milano

Correlatore: Dr. Piervincenzo Rizzo, University of Pittsburgh

Tesi di Laurea di:

Ambra Vandone Matr. 736155

Anno accademico 2010 - 2011

Contents

Sommario

Abstract

Introduction

Acknowledgements

Chapter 1 The infrared thermography	1
1.1 Overview about thermal imaging science	1
1.2 Application in nondestructive testing techniques	2
1.2.1 Review of nondestructive techniques.....	3
1.2.2 Review of infrared based nondestructive techniques.....	4
1.3 Applications in material testing.....	7
Chapter 2 Thermal image processing	9
Chapter 3 Infrared image simulations	19
3.1 Simulations for pulsed thermography.....	19
3.1.1 First simulation: radial heat propagation	20
3.1.2 Second simulation: Gaussian temperature distribution.....	29
Chapter 4 Experimental study	34
4.1 The algorithm	34
4.1.1 ExaminIR environment.....	34
4.1.2 Matlab environment	36
4.2 Laser spot thermography experiments.....	39
4.2.1 System setup	40
4.2.2 First study: unidirectional CFRP plate, detection of surface cracks ..	43

4.2.3	Second study: unidirectional CFRP plate, detection of impact damage	53
4.2.4	Third study: bidirectional GFRP plate, detection of different damages	61
4.3	Tensile test experiments	67
4.3.1	System setup	67
4.3.2	Tensile testing results	69
Chapter 5 Conclusions and future works		80
5.1	Discussion of the results	80
5.2	Future developments	82
5.2.1	Overview about the discrete wavelet transformation	82
5.2.2	Simulations for vibrothermography or thermosonics technique	85
Figures caption		92
Tables caption		96
Acronyms		96
Bibliography		97

Sommario

Col presente lavoro, si propone un algoritmo per l'analisi d'immagini a infrarossi da poter impiegare in tutte quelle applicazioni volte al rilevamento di aree danneggiate in strutture o componenti meccanici. Un primo studio riguarda immagini ottenute da controlli non distruttivi basati sulla tecnica di Laser spot thermography e mira a rilevare la presenza di difetti superficiali. Una sorgente laser è utilizzata per la scansione di un provino attraverso la generazione d'impulsi singoli. La distribuzione di temperatura prodotta da questa fonte termoelastica è misurata attraverso una termocamera a infrarossi e processata con un algoritmo a due stadi. Nella prima fase, si utilizzano semplici parametri matematici e statistici per rilevare la presenza di aree danneggiate. Una volta segnalata la presenza del difetto, si calcola derivata spaziale prima e seconda dell'immagine termica e si applicano due filtri spaziali con l'intento di aumentare il contrasto, individuare e dimensionare il difetto. Tra i vantaggi del metodo proposto rispetto ad approcci esistenti vi sono l'automazione del processo di rilevamento del difetto e un migliore isolamento della zona danneggiata. L'algoritmo è prima testato su immagini termiche ricostruite artificialmente e quindi sperimentalmente validato con la scansione della superficie di una piastra in composito con difetti indotti. Nella seconda applicazione, lo stesso algoritmo è applicato a immagini a infrarossi acquisite durante prove di trazione su campioni di acciaio. Manifestazioni di calore accompagnano la trasformazione elastoplastica durante i test. L'algoritmo, ancora una volta, è in grado di valutare automaticamente lo stato di danneggiamento del campione e di evidenziare l'evoluzione della deformazione.

Parole chiave: Image Processing, Radiazione a infrarossi, Controlli non distruttivi, Laser Spot Thermography, Prove di trazione, Correlazione di segnali, Filtri spaziali.

Abstract

In the present work, an algorithm for the analysis of raw thermal infrared images is proposed and exploited in two different applications: a nondestructive evaluation test and a tensile test. In the first one, the images are obtained by using the laser spot thermography and aim at detecting the presence of surface defects. A laser is used to scan a test specimen through the generation of single pulses. The temperature distribution produced by this thermoelastic source is measured by an infrared camera and processed with a two-stage algorithm. In the first stage, simple mathematical and statistical parameters are used to flag of the presence of damage. Then, once damage is detected, the thermal image's first and second spatial derivative and two spatial filters are computed to enhance contrast, and to locate and size the defect. Some of the advantages of the proposed method with respect to existing approaches include automation in the defect detection process and better defective area isolation through increased contrast. The algorithm is first proven by analyzing simulated thermal images and then it is experimentally validated by scanning the surface of a CFRP composite plate with induced defects.

In the second application, the same algorithm is applied to infrared images recorded during tensile tests on steel samples. Calorific manifestations accompany the elastoplastic transformation during tests. The algorithm, once more, is able to estimate automatically the state of damage of the specimen and to highlight the evolution of the deformation.

Keywords: Image Processing, Infrared Radiation, Nondestructive Evaluation, Laser Spot Thermography, Tensile test, Signal Correlation, Spatial Filtering.

Introduction

Infrared thermography is a technique addressed to the visualization and acquisition of thermal images.

A body capable of absorbing radiation is also capable in the emission of radiation, according to the Kirchhoff's law. This emission is characterized by radiation of wavelength beyond the visible spectrum, and thus, it is called infrared radiation. The total emissive power of a body is measured through the Stefan-Boltzmann's law that states the total radial emittance is proportional to the fourth power of its absolute temperature. Measuring this kind of energy is possible to evaluate the temperature distribution onto the object surface. This can be realized thanks to suitable thermocameras that detect the intensity of the emitted radiations, convert it into digital signals making it possible to display data in numerical or graphical form, thus building the thermal image visible to the naked eye.

Infrared thermography is used in various fields, from clinical diagnostics to industrial preventive and predictive evaluation. In both cases, it is important to reveal oddities and irregularities in the distribution of the analyzed bodies' temperature as these are indicators of anomalous, and therefore undesired, situations. For example, areas of higher temperature than the standard conditions may identify infections or muscle injuries in the medical field, or damaged isolators and overheated joint, signs of incipient failure, in the industrial field.

In the engineering field, this method is widely used for nondestructive evaluation techniques. The nondestructive testing (NDT) is the sum of examinations, tests and surveys accomplished through methods that do not alter the material and do not require the destruction or removal of samples from the structure in question aimed at the detection and identification of structural defects. This kind of tests enables to

evaluate the damage into the analyzed object without impairing its future use. As a result, maintenance and repair costs decrease while safety and reliability increase. Several non-destructive techniques have been developed by the 1920s; each has its own advantages, flaws and areas of application. In the last few decades, the non-destructive techniques based on the infrared thermography (IRNDT) have widely spread. This was possible thanks to the development of accurate devices and their entrance in the market at affordable prices. These methods are able to provide immediate measurements of the temperature without contact. They are therefore widely used in all applications where achieving the test object is physically difficult or dangerous. They are widely used in the control of power lines where, for example, the malfunction of an insulator of a cable can increase the risk of fire. The local overheating of the insulator is shown as a hot spot through the thermal camera, suggesting the operator a maintenance intervention. In the nuclear field, checks on the integrity of the reactors are necessary to ensure safe operation. Given the harmfulness of nuclear radiation, personnel should hold off from machinery. The possibility of performing measurements at a distance brings obvious advantages.

Infrared thermography is commonly exploited also in standard applications such as quality control of mechanical components that undergo several cycles of load with risk of nucleation of fatigue cracks, or damage induced by impacts with external bodies. It is often preferred over other techniques because it enables to inspect large areas very quickly in a completely non-invasive way.

In particular, the present work is addressed to the detection of damages of different nature in different materials through the analysis of raw thermal images acquired from Laser spot thermography. Tests based on this methodology fall into the category of active thermography. An external stimulus is required to create the temperature difference between defect and host material necessary for the detection

of the singularity. In this case, a laser source generates pulsed beams reaching the surface inspected. The energy released produces a local increase in temperature displayed by the camera as a hot spot. Heat tends to propagate in the material equally in all directions (under the assumption of homogeneous material). The presence of a crack or impact damage prevents the lateral heat flow, thereby altering the circular shape of the hot spot. An expert operator that carefully observes each thermogram acquired can detect this asymmetry of the warmer area. Obviously, this procedure is onerous especially in terms of time and subjected by the human error.

The main purpose of this study is therefore the development of an algorithm for the image processing able to locate damaged areas that may be present in the analyzed specimen, in a completely automated way. The images are analyzed in the first instance to extract features to compare with characteristics of sound areas. Only in case of a discrepancy between these parameters, the suspicious frame is processed in order to improve its quality and to highlight the defect signature through spatial filters and balance of contrasts.

The same algorithm is then applied to images relating to proof for the characterization mechanical features on steel samples. The specimen is subject to tensile tests to obtain its stress-strain curve. In parallel, thermal images showing the fracture behavior of the specimen can be acquired. During the deformation, some energy is dissipated as heat right by the area affected by plasticization. Thus monitoring the temperature enables to indicate the evolution of the damaged area. Through the image processing it is possible to assess the specimen's state of damage, to identify the moment of rupture, and to highlight the concentration of temperature around the fracture point.

The presentation of what mentioned above is organized into four chapters. In the first chapter, the main areas of application of infrared thermography are presented, with particular attention to those applications studied experimentally, i.e. Laser spot thermography for the detection of defects in composite materials or Tensile testing for the characterization of high performance steel. In the second chapter, a bibliographic research concerning the state of the art about the image processing is provided, with explanations about the application of filters, histogram equalization, and noise reduction. In the third chapter, the presentation of simulation models on which the algorithm developed in Matlab environment is pre-tested and validated follows. In the fourth chapter, a detailed description of the experimental studies is reported. The results of four different experimental studies are discussed: the first three studies concern the detection of defects of various geometries, types, and sizes through Laser spot nondestructive technique and the last one presents the application of the infrared thermography to traditional tensile tests. Finally, conclusions and observations on experiments and possible further developments of the work done so far are reported.

Acknowledgements

I would like to thank Professor Marcello Vanali that gave me the opportunity to realize the present work in collaboration with the members of the Civil and Environment Department of the University of Pittsburgh.

A special acknowledgement goes to Dr. Piervincenzo Rizzo that guided me in the development of the algorithms and in the conduction of the experiments. He gave me the chance to participate in different research activities and thanks to his enthusiasm, he motivated me to study seriously and conscientiously convinced about the satisfaction that a good research project yields.

A little thought is addressed also to my laboratory mates that shared this experience with me and to all the people that always supported and helped me.

Chapter 1

The infrared thermography

1.1 Overview about thermal imaging science

Infrared thermography, thermal imaging, and thermal video are examples of infrared imaging science. Thermal imaging cameras detect radiation in the infrared range of the electromagnetic spectrum (roughly 9–14 μm) and produce images of that radiation, called thermograms. Since infrared radiation is emitted by all objects above absolute zero according to the black body radiation law, thermography makes it possible to see one's environment with or without visible illumination. The amount of radiation emitted by an object increases with temperature; therefore, thermography allows one to see variations in temperature. When viewed through a thermal imaging camera, warm objects stand out well against cooler backgrounds; humans and other warm-blooded animals become easily visible against the environment, day or night. As a result, thermography is particularly useful to military and other users of surveillance cameras but its use in many different fields has increased dramatically with the commercial and industrial applications of the past fifty years. Government and airport personnel used thermography to detect suspected swine flu cases during the 2009 pandemic. Firefighters use thermography to see through smoke, to find persons, and to localize the base of a fire. Maintenance technicians use thermography to locate overheating joints and sections of power lines, which are a telltale sign of impending failure. Building construction

technicians can see thermal signatures that indicate heat leaks in faulty thermal insulation and can use the results to improve the efficiency of heating and air-conditioning units. Some physiological changes in human beings and other warm-blooded animals can also be monitored with thermal imaging during clinical diagnostics.

Infrared thermography is also used in the engineering field, for instance, in material testing (as tensile tests) or quality control through nondestructive testing (NDT) techniques.

Before the discussion of these two applications in pursuance of the present work, a brief overview about NDT methodologies and material characterization tests is presented below.

1.2 Application in nondestructive testing techniques

In the field of quality control of structures and mechanical components, several methods have been developed to evaluate the integrity or the state of damage of the testing object. Some material investigations involve taking a sample of the inspected part. Due to the loss of material, the test object has to be removed from service permanently. Since 1920s, the art of testing without destroying the test object has developed from laboratory curiosity to an indispensable tool of production. Nondestructive testing has been defined as comprising those test methods used to examine or inspect a part, material, or system without impairing its future usefulness [1]. NDT testing is used to investigate specifically the material integrity of the sample in order to avoid failures, prevent accidents, ensure customer

satisfaction, and even save human life. Several methodologies can be included in this category as discussed below.

1.2.1 Review of nondestructive techniques

Common NDT techniques can be classified into seven major categories: visual (e.g., visual inspection using borescope), penetrating radiation (e.g., X-ray, and neutron imaging), magnetic-electrical (e.g., magnetic particle, and Eddy current), mechanical vibration (e.g., ultrasonic, acoustic emission, and tapping), chemical/electrochemical (e.g., chemical spot testing), thermal (e.g., infrared thermography) and other optical methods (e.g., Moiré´ interferometry, holography, and shearography). Research efforts are being directed at developing and perfecting NDT techniques capable of monitoring: 1) materials production processes, 2) material integrity during transportation, storage and fabrication and, 3) the amount and rate of degradation during service. In addition, efforts are underway to develop new NDT techniques capable of measuring the discontinuity of the flaws quantitatively, permitting determination of material response using fracture mechanics analysis, and replacing the qualitative materials characterization techniques used in the past by quantitative techniques.

Among the various new NDT techniques developed recently, infrared thermography NDT techniques has attracted considerable interest in a wide variety of industries including medical diagnostic, electronic, rubber, aerospace, automotive, and construction. In order to adapt and develop thermography NDT technique for evaluating particular materials, especially for real-time and mass inspection, it is important to have the knowledge of the capabilities as well as limitations of this technique. This methodology is relatively fast, provides full-field

information, is non-contacting, and has been shown to be reliable for detecting material defects in specific metallic, nonmetallic and composites materials [2]. It is based on the analysis of the temperature distribution on the surface of tested sample. It proves not to be suitable if the damage has no effect in perturbing this distribution, for example when the defect lies in depth of a thick specimen.

More details about nondestructive evaluation (NDE) methods based especially on infrared thermography are presented in the next section.

1.2.2 Review of infrared based nondestructive techniques

As mention above, infrared thermography is a contact-less optical imaging technique for detecting invisible infrared radiation. It can be used to assess and predict the structure or behavior lightly beneath the surface by measuring the distribution of infrared radiation and converting the measurements into a temperature scale. Infrared thermography is generally divided into two main streams: passive infrared thermography (PIT) and active infrared thermography (AIT). In PIT, abnormal temperature profiles indicate suspicious problem. This technique is mainly used for qualitative inspection to pinpoint the anomalies and has important applications in several fields such as production process, predictive maintenance, medicine, building thermal efficiency survey programs.

For reducing the sensitivity to variations in ambient condition and obtaining more accurate measurement, AIT has been developed to provide more accurate information by considering the amount of thermal radiation and heat transfer. It has been successfully employed for flaws inspection in many industrial applications, such as aircraft and automotive components inspection, adhesive bonding and spot welding investigations, pressure vessel and pipeline inspections [2]. In Active

thermography, an external stimulus is required to raise the temperature of a part of the structure and generate a heat flow towards colder areas and an infrared camera is utilized to capture the surface thermal pattern. Different techniques have been developed, depending upon the type of external stimulus exploited. The most common thermal stimulation methods in AIT are transient pulse, step heating (long pulse), periodic heating (lock-in), and thermal mechanical vibration. Figure 1.1 provides a schematic representation of these techniques.

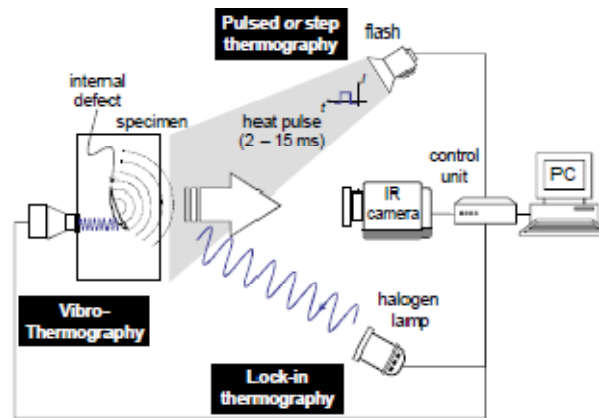


Figure 1.1. Schematization of the data acquisition setup for different stimulation techniques.

The selection of a method over another is dictated by factors as structure geometry and material, and by type and size of the defect to be identified. It has been proved that not every kind of defect can be easily detected using the same technique; and not all the materials respond with success to a particular heating source [3]. To investigate the potentiality of AIT, several studies were conducted and now present in literature.

Pulsed thermography technique often exploits flash lamps to impart thermal energy on the test specimen [3,4,5]. This method has the advantage of being quick and

simple, and suitable to both metallic and non-metallic materials. It is effective for planar defect detection where the defect plane is reasonably parallel to the sample's surface. However, pulse thermography may fail to identify the presence of micro-cracks or of surface breaking cracks that run perpendicularly to the surface because they have little effect on the heat flow generated by the flash lamp [6]. Other active methods such as thermosonics, vibrothermography, or laser spot thermography can be adopted to overcome these limitations.

Thermosonics uses a pulse of high power ultrasound in the 20 – 100 kHz range applied at one point of the test specimen to generate vibration in the structure. If a crack is present, its surfaces rub together causing a local temperature rise. The method is attractive for the quick assessment of complex components [7]. Usually the high power ultrasound is delivered to the structure by means of acoustic horns [7,8,9,10,11,12] or piezoelectric exciters [4,13]. Similar to thermosonics, vibrothermography uses continuous vibration excitation to generate a steady state, local temperature rise [7,8]. This method is particularly effective in poor thermal conductors, so that the temperature does not equalize rapidly over the component [7,10]. Like for thermosonics, the excitation sources are generally acoustic horns or piezoelectric transducers [5,10,14]. In laser spot thermography the external stimulus is given by means of CW or pulsed laser. The laser permits to realize the transmission of a well-controlled and positioned beam into the test object. The heating at the surface, caused by absorption of laser light (CW laser) or by thermoelastic shock (pulsed laser), spreads radially producing a circular heat spot that can be imaged by an infrared camera. Directional patterns can be also induced by interposing a cylindrical lens between the laser and the test specimen. In both cases, the area hit by the laser and the power of the source can be controlled fairly accurately. An argon ion laser yields output of few watts, whereas carbon dioxide

laser and neodymium-yttrium aluminum garnet laser can provide output power in excess of 20 W if necessary. A surface breaking crack near to the illumination point prevents the lateral flow of heat and produces a perturbation to the thermal image that can be useful to detect the presence of such cracks [6,8,15,16]. An application of this methodology for the detection of surface damages is discussed in the following chapters.

1.3 Applications in material testing

Tensile testing, also known as tension testing, is a fundamental materials science test in which a sample is subjected to uniaxial tension until failure. The results from the test are commonly used to select a material for an application, for quality control, and to predict how a material will react under other types of forces. Properties that are directly measured via a tensile test are ultimate tensile strength, maximum elongation, and reduction in area. From these measurements, the following properties can also be determined: Young's modulus, Poisson's ratio, yield strength, and strain-hardening characteristics.

Recently the infrared thermography has been coupled to the traditional tensile testing measuring devices to investigate the fracture behavior and monitor failure mode during the test. [17]

Infrared thermography provides quantitatively evaluation of the evolution of the temperature generated by the specimen under applied stresses. It has been successfully used as an experimental technique to detect the plastic deformation of steel plates under monotonic loading. The work done to the system by plastic deformation (evaluated, per unit of volume, by integrating the material stress-strain

curve) is identified as the major contribution to heat effect. There exists a general acceptance that not all mechanical work produced by the plastic deformation can be converted to the thermal energy in the solid. A portion of the work is believed to have been spent in the change of material microscopic structure.

Thus, the material dissipativity can be considered and used as a highly sensitive and accurate manifestation of damage. Infrared thermography provides a nondestructive, real time and noncontact technique to observe the physical processes of degradation and to detect the occurrence of intrinsic dissipation in engineering materials and structures [1]. The application of the above-mentioned technique is discussed in the forth chapter where the heat pattern on the surface of a steel sample shows the evolution of the damage until failure.

Chapter 2

Thermal image processing

For the sake of completeness, it must be remembered what an infrared radiation concerns and how an infrared image can be processed.

Infrared (IR) light is electromagnetic radiation with a wavelength longer than that of visible light, measured from the nominal edge of visible red light at 0.7 micrometers, and extending conventionally to 300 micrometers. These wavelengths correspond to a frequency range of approximately 430 to 1 THz, and include most of the thermal radiation emitted by objects near room temperature [18]. Figure 2.1 shows the electromagnetic spectrum for different types of radiations.

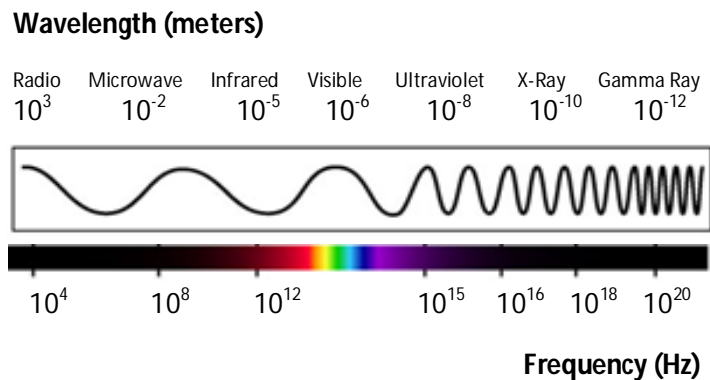


Figure 2.1. Classification of the electromagnetic radiations according to their wavelength and frequency.

Infrared thermography in nondestructive testing provides images (thermograms) in which zones of interest (defects) appear sometimes as subtle signatures due to all

factors that degrade infrared images from self-emission of the IR camera to the nonuniform properties of the surface where data are collected. Moreover, with long wavelengths in IRthermal bands with respect to visible bands, signals in the thermal bands are intrinsically weak since liberated photonic energy W due to the oscillatory nature of particles inside matter is inversely proportional to the wavelength. In this context, raw images are not always appropriate since some details can be missed. In some other cases, what is needed is a quantitative analysis such as for defect detection and characterization.

From years to years, various methods of data analysis in IRNDT have been developed through the world [19]. Most of the existing methods require user input or intervention, and automation is not always possible. The most common steps in infrared image processing can be listed as follow:

- Noise reduction: to augment the signal to noise ratio;
- Contrast balance: to highlight some features not evident in the original image;
- Edge detection: to define the discontinuities in the frame considered.

One of the most common procedures for noise reduction is the subtraction technique. Simple subtractions such as subtracting two images acquired at the same moment from two different experiments (spatial reference technique) or from images recorded closely (temporal reference technique) allow to remove unwanted effects present in both experiments such as non-uniform heating [4,7,9,10,14,20].

Moreover, the application of spatial linear or nonlinear filters is often exploited to reduce the high-frequency components characterizing thermal noise [9,20,21]. Applying a linear filter means computing the convolution onto the image considered of a defined kernel, which is a square small matrix with an odd number

of elements. In the spatial domain, the convolution process multiplies the elements of the kernel by the matching pixel values when the kernel is centered over a pixel. The elements of the resulting array (which is the same size as the kernel) are averaged, and the original pixel value is replaced with this result. In particular, a kernel $(n+1 \times n+1)$ is passed through the image and the central pixel value p is replaced by p_0 computed as follow:

$$p_0 = B(a_1 p_1 + a_2 p_2 + \dots + a_{(n+1)^2} p_{(n+1)^2}) \quad (2.1)$$

with B is a scaling factor, a_i are kernel weights and p_i are the $n+1$ pixel values within the kernel centered on p [19].

The mechanics of the linear spatial filtering are illustrated in Figure 2.2. Linear spatial filtering application Figure 2.2.

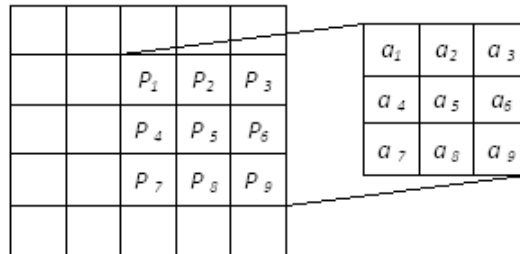


Figure 2.2. Linear spatial filtering application.

Nonlinear filters exploit the same mechanism but the relation between the value of the central pixel p and its replacing value p_0 is not linear.

Spatial filters can also be applied to enhance the defect signatures. For instance, Li et al. [21] proposed a three-dimensional matched filter (time is the third dimension) to detect cracks from a video sequence collected during a vibrothermographic

inspection. The use of a matched filter required the knowledge of the signal signature. As such, Li and collaborators [21] applied a matched filter assuming that the heat change signature due to the presence of cracks was known. To avoid this problematic aspect, it is possible to act on image histograms and contrasts. These procedures deal with images in gray scale; procedures for color images derive from them. Each pixel can assume one of 256 possible values: a value equal to zero correspond to the black color, a value of 255 correspond to the white color.

An image histogram is a type of histogram that acts as a graphical representation of the tonal distribution of the picture. It plots the number of pixels for each tonal value. By looking at the histogram for a specific image a viewer is be able to judge the entire tonal distribution at a glance and eventually to identify the presence of a particular kind of noise on the picture. Adjusting the tonal distribution, noise can be reduced and certain details can be better visualized. A common procedure is the histogram equalization that generates an image whose intensity levels are equally likely. The net result is an image with increased dynamic range which tends to have higher contrast [22]. Figure 2.3 presents an example of the above.

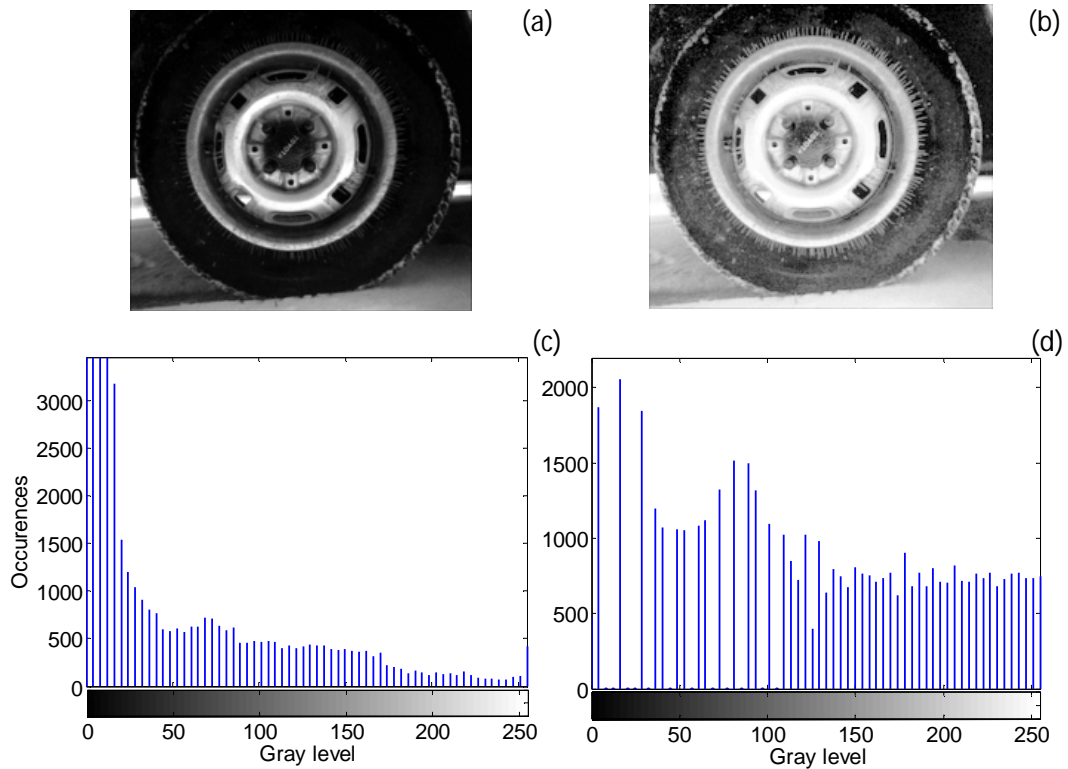


Figure 2.3. Original image (a) and correspondent histogram (c). Enhanced image (b) and correspondent histogram (d).

The last step mentioned above concerns the edge detection technique. This procedure is most exploited in IRNDT methods since it is often required to localize and size the damaged area in the testing sample. The techniques for the extraction of the contours, aim to remove from the image constant areas, leaving only the changes, in the case, often verified, that they retain all the relevant information. Contours are defined as local discontinuities in luminance, i.e. areas in the image where there are "abrupt" changes in luminance. These techniques can be divided in three main categories based on first derivative, second derivative and edge fitting.

The techniques based on the derivatives are the most effective and thus the most exploited. The goal of the method based on the first derivative is to pick out the maximum values of this feature.

Figure 2.4 shows a possible intensity trend $f(x)$ as a function of the spatial coordinate x .

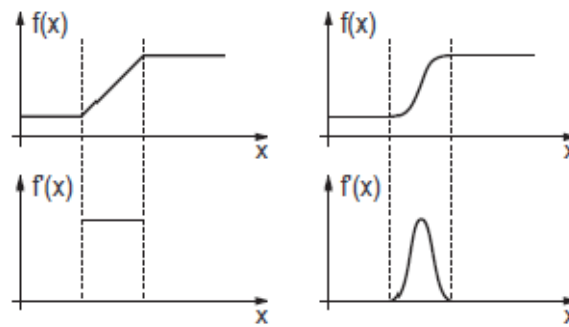


Figure 2.4. Intensity functions in correspondence of two different types of edges and corresponding first derivatives.

The ramp indicates a change in the luminance level that leads to the identification of a contour. The first derivative is calculated as:

$$f'(x) = \frac{df(x)}{dx} \quad (2.1)$$

The peak corresponding to the maximum absolute value of $f'(x)$ occurs in correspondence of the contour. Of course, in presence of noise there are several local maximum values; some of them related to real contours but some others related to the noise effect. Thus, it is possible to set a threshold level: peaks below this reference value are defined as “false” contours and not considered.

In the discrete domain, the first derivative of a sequence of intensity values $x(n)$ is calculated as follow:

$$x'(n) = \sum_{k=-\infty, k \neq 0}^{\infty} \frac{(-1)^k}{k} x(n-k) \quad (2.2)$$

For instance:

$$x'(10) = x(11) - x(9) + \frac{x(12)}{2} - \frac{x(8)}{2} + \frac{x(13)}{3} - \frac{x(7)}{3} + \dots \quad (2.3)$$

In practice the sum is cut off and the result is approximated as illustrate below.

Extending into the second dimension this concept, the gradient is considered:

$$G(x, y) = \left(\frac{\delta}{\delta x}, \frac{\delta}{\delta y} \right) \quad (2.4)$$

The magnitude of this vector stands for the “strength” of the contour and the phase indicates the direction. In the discrete case, the gradient is calculated along the rows or along the columns of the matrix representing an image, and then, combined as:

$$G(i, j) = \sqrt{G_r^2(i, j) + G_c^2(i, j)} \quad (2.5)$$

An approximation often used of Equation 1.6 is:

$$G(i, j) = |G_r(i, j)| + |G_c(i, j)| \quad (2.6)$$

G_r and G_c are estimated according to Equation 2.3 regarding the discrete first derivative stopped at the second term. In other words, it is calculated as the response of an impulse of the type $[-1 \ 0 \ 1]$. This procedure is very sensitive to the noise. For a more stable solution, a common method is to average in the orthogonal direction before calculating the difference. Table 2.1 shows examples of suitable operators for this procedure.

Table 2.1. Masks for edge detection

	Gradient for rows	Gradient for columns
Prewitt	$\frac{1}{3} \begin{bmatrix} 1 & 0 & -1 \\ 1 & 0 & -1 \\ 1 & 0 & -1 \end{bmatrix}$	$\frac{1}{3} \begin{bmatrix} -1 & -1 & -1 \\ 0 & 0 & 0 \\ 1 & 1 & 1 \end{bmatrix}$
Sobel	$\frac{1}{4} \begin{bmatrix} 1 & 0 & -1 \\ 2 & 0 & -2 \\ 1 & 0 & -1 \end{bmatrix}$	$\frac{1}{4} \begin{bmatrix} -1 & 2 & -1 \\ 0 & 0 & 0 \\ 1 & 2 & 1 \end{bmatrix}$
Roberts	$\begin{bmatrix} 0 & 0 & 0 \\ 0 & -1 & 0 \\ 0 & 1 & 0 \end{bmatrix}$	$\begin{bmatrix} 0 & 0 & 0 \\ 0 & -1 & 1 \\ 0 & 0 & 0 \end{bmatrix}$

A practical application of these masks is presented in the next chapters. In literature, several studies exploited the edge detection based on the first derivative. For instance, T. Li et al. [16] used a crack imaging method to process infrared images collected by means of the laser spot thermography. The image processing was based on the computation of this spatial derivative since it reflects the amplitude change rate in an image. Furthermore, they evaluated the second derivative to better enhance the edge effect.

Methods based on the second derivative seek for the passages of the function $f''(x)$ for values equal to zero that occur in correspondence of the boundary. Figure 2.5 helps in visualizing the concept:

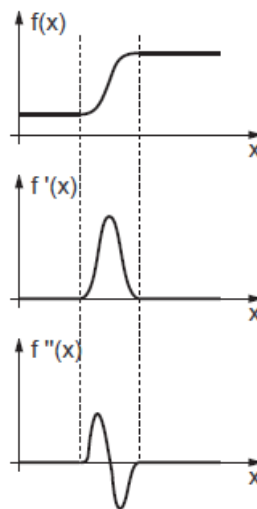


Figure 2.5. Intensity function in correspondence of an edge and its first and second derivative.

The second derivative is sensitive to the noise so that some zero values can be dictated by the noise effect. A strategy to avoid the “false” boundary is to take into account only the zeros surrounded by “high” absolute values (maximum and minimum). Working in two dimensions, the second derivative becomes the Laplace operator, defined for a continuous function $F(x, y)$ as:

$$G(x, y) = -\nabla^2 F(x, y) = \frac{\partial^2}{\partial x^2} F(x, y) + \frac{\partial^2}{\partial y^2} F(x, y) \quad (2.7)$$

The Laplacian is equal to zero when $F(x, y)$ is constant or changes linearly.

In the discrete domain, the easiest way to evaluate this operation is to compute the difference of the differences along each direction as follow:

$$G(j, k) = [F(j, k) - F(j, k - 1)] - [F(j, k + 1) - F(j, k)] + \\ + [F(j, k) - F(j + 1, k)] - [F(j - 1, k) - F(j, k)] \quad (2.8)$$

The same result can be obtained through the convolution with a matrix $H(j, k)$ defined in Equation 2.11:

$$G(j, k) = F(j, k) * H(j, k) \quad (2.9)$$

$$H = \begin{bmatrix} 0 & 0 & 0 \\ -1 & 2 & -1 \\ 0 & 0 & 0 \end{bmatrix} + \begin{bmatrix} 0 & -1 & 0 \\ 0 & 2 & 0 \\ 0 & -1 & 0 \end{bmatrix} \quad H = \begin{bmatrix} 0 & -1 & 0 \\ -1 & 4 & -1 \\ 0 & -1 & 0 \end{bmatrix} \quad (2.10)$$

The sum of the two matrices yields the evaluation of the second derivatives along the rows and the columns.

In the next chapters of the present work, it is possible to appreciate the effectiveness of this operator since it is able to highlight the discontinuities in the thermal distribution on the surface tested both in the laser spot thermography application and in the tensile tests. These discontinuities represent the anomalous situations that we are looking for while testing a sample.

Chapter 3

Infrared image simulations

In order to become more familiar with the image processing, we conduct a preliminary study exploiting the Matlab software and, in particular, the Image acquisition, the Image processing and the Wavelet toolbox. This study helps us in acquiring more awareness about the potentiality of the commands reported in dedicated Matlab environment. It leads to a conscious management of a two dimensional (2D) signal such as matrices representing the thermal images.

We provide two types of simulations, both with the aim of realizing an algorithm for the image processing of thermographs. In particular, the first model simulates the temperature trend on the sample surface subjected to a generic pulsed thermography testing. The second one tends to recreate the reaction of a sample tested with laser spot thermography technique. The two models are presented in details in the next sections.

3.1 Simulations for pulsed thermography

In this section, we present two models consisting of recreated videos or snapshots to simulate the acquisition of thermal images from pulsed thermography testing. The first situation represents the radial heat propagation from a central point toward the extremes. It is realized by generating consequential frames characterized by

incremental temperature steps. The second situation represents the ideal Gaussian temperature distribution generated onto a surface hit by a laser beam. The laser is mainly exploited in the NDT techniques based on the pulsed thermography.

This kind of testing usually requires user input or intervention to evaluate the integrity of the specimen through the observation of single frames or surface temperature trends as a function of the time (heating and cooling transient). Our goal is to write an algorithm able to detect automatically the presence of a defect and to process only the thermal frames marked as suspicious. In particular, the study yields to the realization of a two-stage algorithm. In the first stage, it evaluates simple mathematical and statistical parameters used to warn of the presence of damage. Then, once damage is detected, it computes the thermal image's first and second spatial derivative and two spatial filters to enhance contrast, and to locate and size the defect. Some of the advantages of the proposed method with respect to existing approaches include automation in the defect detection process and better defective area isolation through increased contrast.

Details and results from this image processing are reported below.

3.1.1 First simulation: radial heat propagation

In this preliminary study, we carry out a basic simulation in order to calibrate the image processing. We recreate five video sequences composed of 14 frames each. These movies represent the heat flow starting from a central point and propagating in both directions (vertical and horizontal) towards the extremes of the image. In particular, the first movie is associated with a baseline situation, and the remaining four are related to four damage scenarios, namely small 45° crack, large 45° crack, horizontal crack, and vertical crack. Figure 3.1 shows six consequential frames of the baseline video.

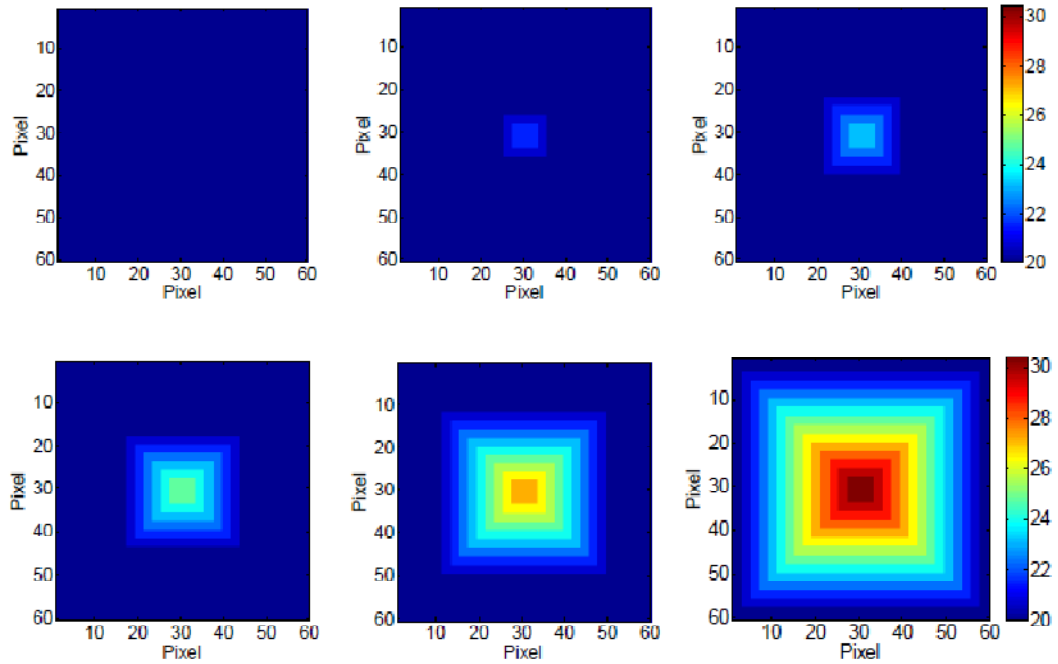


Figure 3.1 First simulation. Six frames of the video sequence associated with no damage case.

The temperature of the object increases progressively according to a square pattern. The temperature increment is of 0.8° Celsius at each step. The other four sequences (testing images) consist of similar temperature patterns. After few frames, we simulate the presence of a defect. Figure 3.2 shows the 14th frame for these four scenarios.

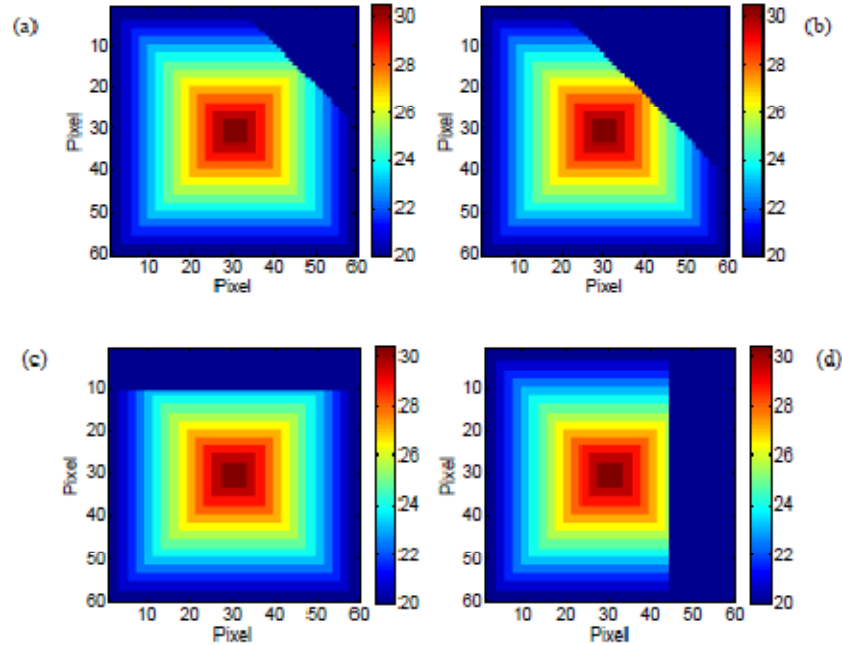


Figure 3.2. First simulation. Last frames of the four video sequences that simulate the presence of damage. (a) Small 45° defect. (b) Large 45° defect. (c) Horizontal defect. (d) Vertical defect.

Note that the presence of damage would create a local temperature increase in the proximity of the damage itself. For the sake of simplicity, we decide not to simulate this temperature rise.

We extract from each frame of each movie the eccentricity value.

The eccentricity e of an arbitrary 2-D boundary is defined as:

$$e = \sqrt{1 - \frac{b^2}{a^2}} \quad (3.1)$$

In Equation 3.1, a is the line segment connecting the two farthest points of the boundary, and b is the line segment perpendicular to a and of such length that a box passing through the outer four points of intersection of the boundary with the two

line segments completely encloses the boundary [22].

This parameter is usually exploited to estimate the similarity of a boundary to a perfect circle. In our study, we calculate the eccentricity value using the Matlab command *regionprops* and retrieving the property “*Eccentricity*”.

It assumes values between 0 and 1. In particular, for a circular shape the eccentricity value is equal to zero.

In laser spot thermography the eccentricity can be used to represent a measure of how much the thermal spot on the testing specimen deviates from being circular irrespective of the thermal distribution within the spot. (This concept is discussed in detail in the next simulation). For the present simulation, we expect a value equal to zero for the eccentricity regarding all the baseline frames. In fact (see Equation 3.1), a and b present the same length since they correspond to the two perpendicular diagonals of the square pattern. In presence of defect, the square shape is cut off and thus, the eccentricity value is expected to be closer to 1.

In image processing, the correlation coefficient is used to establish a relationship between two or more images. One of the principal applications is in the area of template or prototype matching, where the closest match between a test image and a reference image is sought. The closest match can be found by choosing the image that yields the largest correlation value [21]. In literature, several correlation coefficients establish the degree of correlation. One of the most common is the Pearson coefficient, which assesses the linear relationship between two variables. It is defined as:

$$\rho_{X,Y} = \frac{\text{cov}(X,Y)}{\sigma_X \sigma_Y} = \frac{E[(X - \mu_X)(Y - \mu_Y)]}{\sigma_X \sigma_Y} \quad (3.2)$$

where $cov(X, Y)$ is the covariance of random variables X and Y , σ_X and σ_Y are their standard deviations, E is the expected value operator, and μ_X and μ_Y are the means of the two variables.

The correlation coefficient $\rho_{X,Y}$ can assume values between -1 and 1. It is equal to 1 when a linear positive relationship exists between the two variables: if a variable increases, the other one increases proportionally. It is equal to -1 (anticorrelation) when a linear negative relationship occurs between the two variables: if a variable increases, the other decreases proportionally. It is equal to zero when there is no tendency for the values of a variable to increase or decrease with the values of the second variable.

For a series of n measurements, Equation 3.2 can be rewritten as:

$$r_{xy} = \frac{\sum_{i=1}^n (x_i - \bar{x})(y_i - \bar{y})}{(n-1)s_x s_y} = \frac{\sum_{i=1}^n (x_i - \bar{x})(y_i - \bar{y})}{\sqrt{\sum_{i=1}^n (x_i - \bar{x})^2 \sum_{i=1}^n (y_i - \bar{y})^2}} \quad (3.3)$$

where x_i and y_i ($i = 1, 2, \dots, n$), \bar{x} and \bar{y} and s_x and s_y are respectively the measures, the means and the standard deviations of X and Y . When the variables are two-dimensional such as images, Equation 3.3 becomes:

$$r = \frac{\sum_m \sum_n (A_{mn} - \bar{A})(B_{mn} - \bar{B})}{\sqrt{(\sum_m \sum_n (A_{mn} - \bar{A})^2)(\sum_m \sum_n (B_{mn} - \bar{B})^2)}} \quad (3.4)$$

where A and B are two images represented by two matrices, and \bar{A} and \bar{B} are respectively the means of elements of the elements populating matrix A and matrix B . In the framework of our algorithm, we expected correlation coefficients close to 1 for tested regions with no damage and low correlation values for damaged areas.

Figure 3.3a and Figure 3.3b show the correlation and the eccentricity, respectively,

for the five sequences simulated.

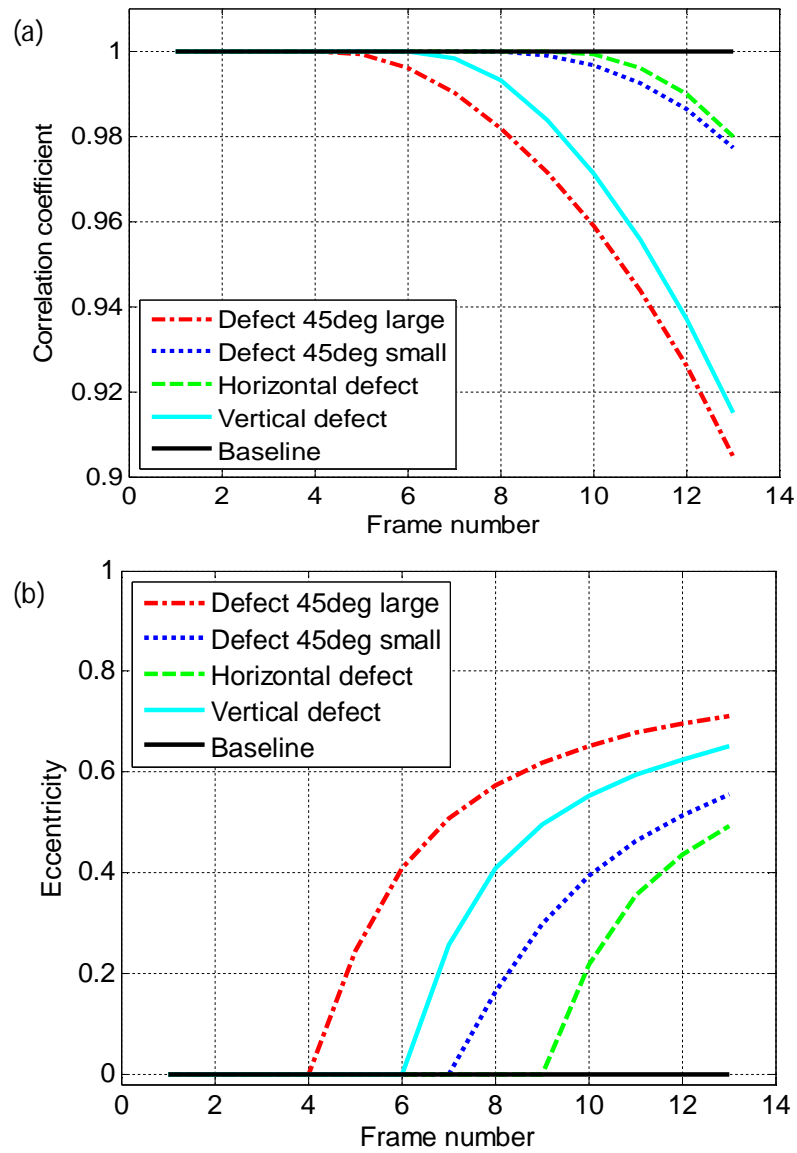


Figure 3.3. First simulation. (a) Correlation coefficient and (b) eccentricity associated with the frames of the five video sequences.

The correlation coefficient of the testing frames is computed by correlating each frame to the correspondent frame of the baseline. For both parameters the presence of damage is readily detected. Baseline frames have all eccentricity equal to zero and correlation equal to one (auto-correlation). All the frames associated with damage denote an eccentricity greater than zero. The highest value (0.71) refers to the last frame of the large 45° crack. Similar trend is noticeable for the correlation coefficient.

In the second stage, the proposed algorithm processes those images whose correlation or eccentricity deviate from the baseline. The first and the second spatial derivatives are calculated by evaluating the image thermal gradient across two consecutive pixels along the horizontal and the vertical axis. The first derivative reflects the amplitude change rate in an image and thus extracts the edge effect in an image. However, in the future perspective to apply the algorithm in pulsed thermography testing, the second derivative is preferable as it can further enhance the edge effect. As pointed out by Li et al. [16,24], in laser spot thermographic images the background heat flow caused by the laser spot is still strong and mixed together with the crack when the spot is close to the crack. Thus, the second derivative provides higher values and then a more evident visualization of the damaged area. Figure 3.4 shows the derivatives along the coordinate axes of the first frame (the sixth) that had both parameters significantly different from the baseline values relatively to the large 45° defect case.

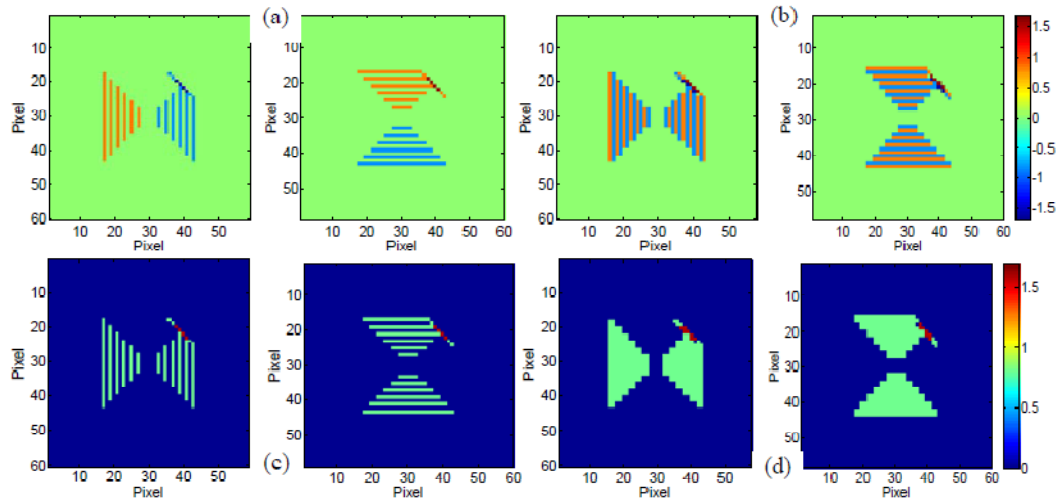


Figure 3.4. First simulation. Spatial derivative of the fifth frame of the sequence that simulate the presence of the large oblique crack. (a) First derivative along horizontal and vertical direction. (b) Second derivative along horizontal and vertical direction. (c) Absolute values of plots in (a). Absolute values of plots in (b).

The contours of the largest derivatives unfold the position and the size of damage. Since the defect was skewed at an angle of 45° , the derivatives in the vertical and horizontal direction yield to the same results. The horizontal and vertical grids visible in the figures are numerical artefacts due to the temperature edges of the original simulated images. It should be noted that the values of these grids are smaller than the values of the crack's edges. Not shown here, the derivatives of the images having higher eccentricity and smaller correlation yield to similar results. In order to highlight the contour of the defected area, we also propose to apply two image filters. In particular, we applied the Roberts and the Laplacian filters as they provide good results. The first filter belongs to the category of directional filter and it is suitable for enhancing the edges at 0° , 45° , 90° , ... The kernel associated with the Roberts filter is [23]:

$$\mathbf{R} = \begin{bmatrix} 0 & 0 & 0 \\ 0 & -1 & 0 \\ 0 & 1 & 0 \end{bmatrix} \quad (3.5)$$

The Laplacian filter is used to compute the second derivatives of an image to determine the presence of edges in adjacent pixels. The kernel for this filter is [21]:

$$\mathbf{L} = \begin{bmatrix} 0 & -1 & 0 \\ -1 & 4 & -1 \\ 0 & -1 & 0 \end{bmatrix} \quad (3.6)$$

Figure 3.5 presents the images obtained from the Laplacian and the Roberts filters associated with the last frame of the large oblique crack.

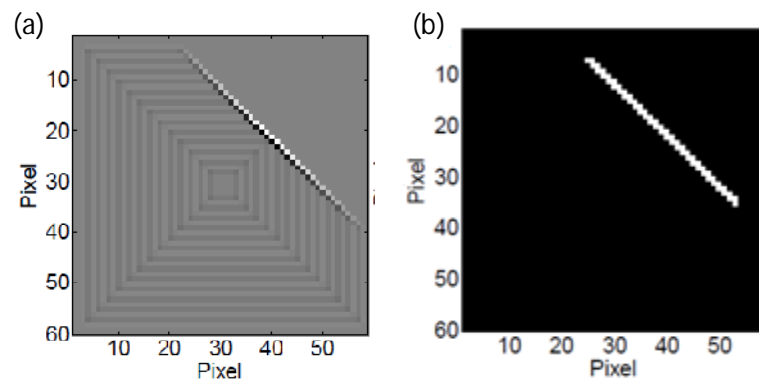


Figure 3.5. First simulation. Results of the (a) Laplacian and (b) Roberts filter applied to the 13th frame of the sequence associated with the large oblique defect.

Both filters show the location of damage clearly. The results presented in the previous figures clearly demonstrate the capability to identify the position and the size of the crack.

3.1.2 Second simulation: Gaussian temperature distribution

In the second simulation, we assumed a Gaussian temperature distribution of a test specimen. This simulation intended to move closer to the experimental setup, discussed in the next chapter, where an unfocused laser beam has a nominal Gaussian distribution of the pulse's intensity.

Figure 3.6*a* shows the temperature distribution of the surface of a pristine specimen. Similarly to the first simulation, we assumed the presence of a vertical crack that prevented the propagation of the heat flux along a certain direction. Under this scenario, we simulated the temperature distribution like the one presented in Figure 3.6*b*. Figure 3.6*c* is the projection of Figure 3.6*a* and it simulates the thermal pattern imparted by a Gaussian laser pulse onto a homogeneous material. Similarly, Figure 3.6*d* is the projection of Figure 3.6*b*.

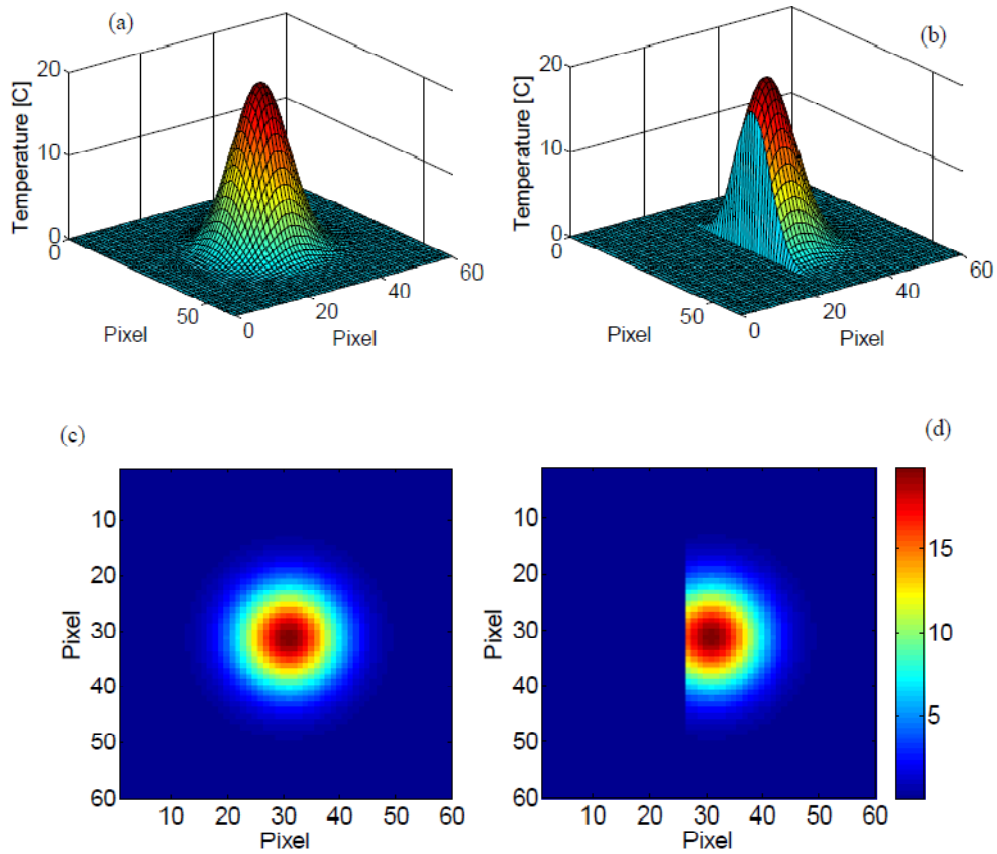


Figure 3.6. Second simulation. (a) Gaussian temperature distribution over a flat pristine surface. (b) Gaussian temperature distribution over the same surface having a vertical defect. (c) Simulated thermal image of (a). (d) Simulated thermal image of (b).

Table 1 shows the values of the correlation coefficients and the eccentricity associated to both cases. We remember that an eccentricity equal to zero corresponds to a perfect circle, given that a and b have the same length (see Equation 3.1). Any deviation from this shape can be inferred to the presence of a structural anomaly, and the value of the eccentricity is expected to increase.

Table 1 - Values of the correlation coefficient and eccentricity for the Gaussian thermal surface distribution.

	Baseline	Damage
Correlation coefficient	1	0.9103
Eccentricity	0	0.7664

Both parameters indicate the presence of a structural anomaly since they depart from the reference values.

Once the presence of a defect was ascertained, the image processing was applied to visualize the location and the size of the defect. Figure 3.7 presents the first and second derivatives of both images and the location of damage is visible. As the defect extended along the vertical direction, the spatial derivatives along the horizontal axis are more sensitive.

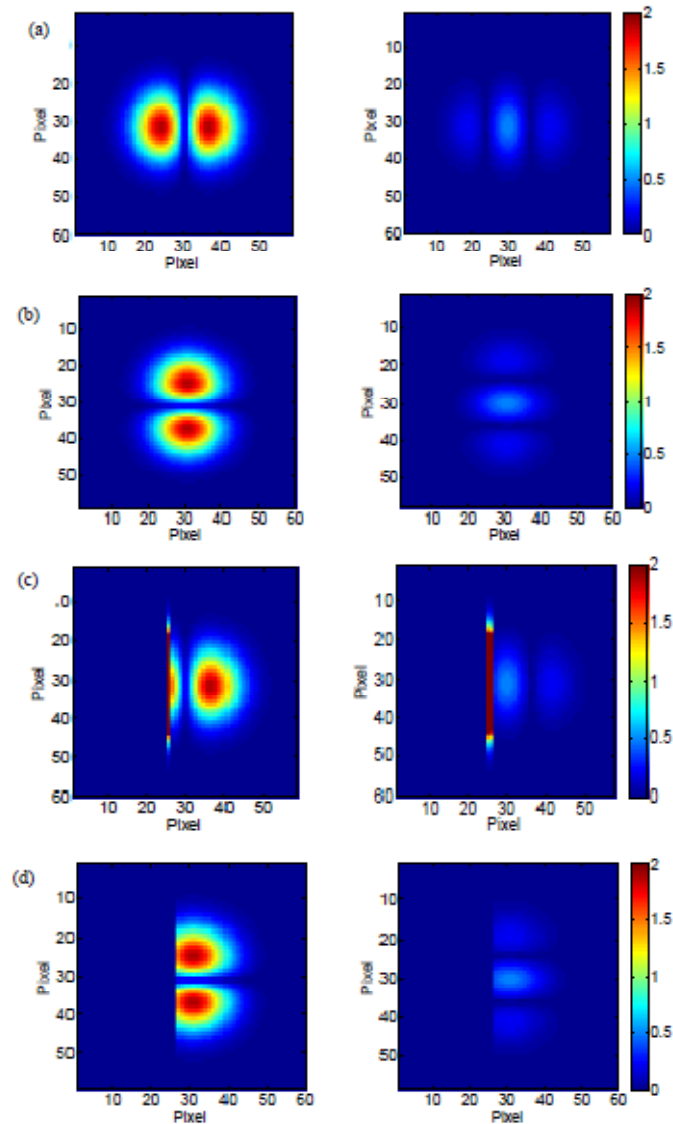


Figure 3.7. Second simulation. (a) First and second derivative along the horizontal axis for undamaged case. (b) First and second derivative along the vertical axis for undamaged case. (c) First and second derivative along the horizontal axis for the case with damage. (d) First and second derivative along the vertical axis for the case with damage.

Finally, Figure 3.8 illustrates the image of the damaged specimen processed with the Laplacian (Figure 3.8a) and Roberts (Figure 3.8b) filters.

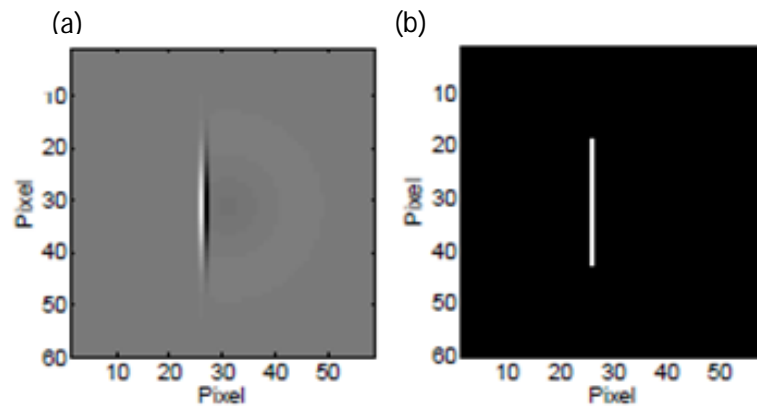


Figure 3.8. Second simulation. Results of the (a) Laplacian and (b) Roberts filter applied to the “damaged” surface.

These filters seem to outperform the spatial derivatives in terms of contrast enhancement. With respect to Figure 3.4 and Figure 3.5a, Figure 3.7 and Figure 3.8a do not have the vertical and horizontal grids that were, as is said earlier, numerical errors due to the step-wise temperature distribution simulated in the first example.

Chapter 4

Experimental study

In the present chapter, we present some experimental studies carried out at the laboratory of the Civil and Environmental Department of the University of Pittsburgh.

First, we propose three different experiments based on laser spot thermography technique with the purpose of detecting surface damages through the application of the algorithm validated in the last chapter. Then, we show the application of the same algorithm in tensile testing experiments with the aim of monitoring the failure behavior of thin samples.

4.1 The algorithm

The next two sections recall the principal steps computed by the algorithm for the image processing.

Two work environments are used: the ExaminIR software for the acquisition and exportation of the data and the Matlab software for the analysis.

4.1.1 ExaminIR environment

Once the system setup is prepared, the camera must be connected to the computer through a firewire cable. The ExaminIR software must be opened and, before

starting the data acquisitions, few object parameters must be set. Instructions for their evaluation are showed in Table 4.1.

Table 4.1. Object parameters, setting instruction and unit of measurement

Parameter	How to set	Units
Reflected temperature	<p>The reflected temperature is the apparent temperature recorded on the sample surface due to the reflection of some radiation coming from the surrounding. This radiation can alter and even invalidate the measurement. Thus for a correct acquisition, it is necessary to take it into account. The FLIR User's manual [24] provides an easy method to estimate this reflected temperature. It briefly states:</p> <ul style="list-style-type: none"> ○ crumble up a large piece of aluminum foil; ○ uncrumble it and put it in front of the sample facing the camera; ○ set the emissivity to 1 and measure the temperature. ○ Set this value as reflected temperature in the camera settings. 	[°C]
Emissivity	<p>The importance of this parameter is discussed above. However, it is possible to consult tabulated values available in literature for different materials at different temperatures. For more accurate measurements, it is possible to set the own emissivity value following the procedure described in the FLIR User's manual [24]:</p> <ul style="list-style-type: none"> ○ attach a piece of electrical tape of known emissivity (usually around 0.97) onto the specimen; ○ set the emissivity mentioned above in the camera device, focus and write down the tape temperature; ○ assuming that the tape and the specimen are in condition of thermal equilibrium, point now to the sample surface and change the emissivity setting until 	--

	the camera displays the same temperature as the one previously recorded.	
Humidity	The presence of water into the atmosphere has effect in the absorption of the radiation emitted by the specimen. Anyway, if no humidity instruments are available, it is possible to set the value at 50%.	--
Distance object - camera	The distance between the specimen and the camera lens is doable easily by means of a ruler. See the technical data sheet for the camera lens in order to respect the minimum focal length.	[m]
Atmosphere temperature	The temperature of the atmosphere normally has not a big influence, assuming of working in standard conditions (-20 to 400 °C). The estimation is very simple and can be done using a common thermometer or reading the room thermostat display.	[°C]

Three other parameters must be set. They regard the acquisition features, and they are acquisition time, frame rate (frequency) and window size. The smaller the window size is, the higher the frame rate can be.

At this point, video acquisitions can be recorded, saved and exported as movies or as multiple separated images in *jpg* or *csv* (comma separated value) format. A single video is recorded for each scanning point and the data set is stored in the corresponding folder, ready to be elaborated by the Matlab scripts.

4.1.2 Matlab environment

The data analysis and the image processing are completely performed with the Matlab software. Eight consequential steps are planned and reported in the block

diagram below. The algorithm can be divided in two stages. The first one regards the evaluation of mathematical and statistical parameters (step 1 to 6). The second regards the image enhancement (step 7 and 8).

Step 1	Load the data set for the video acquisition considered.
Statistical parameters	Compute four statistical parameters for each frame of the video: average temperature of the entire frame, standard deviation, skewness and kurtosis coefficient. (Skewness and kurtosis are measures of outliers of a sample of data. They present a spike in those frames where the hot laser spot is evident).
Starting excitation instant	
Laser spot coordinates	
	Estimate the coordinates of the laser spot center extracted from the <i>first shot frame</i> .

Step 2	Create the so-called <i>cold frame</i> by computing the 2D mean of a hundred frames before the excitation starts. This is done with the aim of reducing the thermal noise and creating a reference frame representing the background temperature distribution in normal condition (no laser excitation).
“Cold” reference frame	

Step 3	Cut out a small region of interest from the entire frame keeping the center of the laser spot (of know coordinates, see Step 1) in the middle of the ROI (region of interest). This step helps in the computational time.
ROI cut out	

Step 4	Load the sequences of images surely regarding sound areas. Calculate the first shot frame for each baseline video. Compute the 2D mean between the different acquisitions for each frame after the first shot one with the aim of reducing the thermal noise and recreating a reference video, named <i>baseline video</i> .
Baseline reference video	

Step 5	Load the data set for the acquisition correlated to the scanning point considered.
Correlation	Compute the correlation coefficient comparing the <i>first shot frame</i> of the data sequence considered and the one selected from the <i>baseline video</i> (Matlab command: <i>corr2</i>). If the correlation coefficient lies below a fixed threshold then mark the acquisition as suspected.

Step 6	Load the data set for the acquisition correlated to the scanning point considered.
Eccentricity	Compute the eccentricity of the laser spot (Matlab command: <i>regionprops</i>). Compare this parameter to the eccentricity regarding the <i>first shot frame</i> of the <i>baseline video</i> . If the value lies below a fixed threshold then mark the acquisition as suspected.

Step 7	Load the data set from the acquisition marked as suspicious.
Derivatives	<p>Compute the first and second derivatives of the <i>first shot frame</i> in both directions, vertical and horizontal.</p> <p>Visualize the gradients in color scale images to better visualize the damaged area.</p>

Step 8	Load the <i>first shot frame</i> of the flagged acquisition and apply the Roberts and Laplacian spatial filter (Matlab command: <i>imfilter</i>).
Filtering	Visualize the results in gray scale images to highlight the defect edges.

Next sections show a practical application of the above and the results obtained for laser spot and tensile testing.

4.2 Laser spot thermography experiments

We report two tests conducted onto a unidirectional carbon fiber plate and one test regarding a bidirectional glass fiber reinforced composite material widely used in the aeronautic industry.

Following we provide the description of the experimental setup with details about the main devices and the explanation of the problems related to the acquisition of the images. Then, we show the experimental results.

4.2.1 System setup

A unidirectional carbon fiber plate of dimensions 605 x100 x 2 mm and a bidirectional glass reinforced composite plate of dimensions 600 x300 x 3 mm are inspected. Surface damages were previously performed by means of a cutter or by the impact of a falling mass onto the plates. For each test, the specimen is fixed to a marked horizontal guide to ease the scan of the specimen. For each scanning point, few seconds sequences are recorded in order to capture enough information about the temperature distribution prior and after the release of the laser pulse.

A 10 Hz repetition rate Nd:YAG pulse laser operating at 1064 nm wavelength and intensity equal to 3.85 mJ/mm² is used to impart a single 8 nanosecond 7 mm diameter pulse on the test specimen. The use of a large circular spot instead of a focused line or point as conventionally done in laser-spot thermography [6,8,15,16] allows to increase the scanning speed because the region of interest (ROI) associated with each scanning point is greater.

The infrared images are recorded with a FLIR SC660 camera with an aSi (amorphous silicon) infrared detector and thermal sensitivity (NETD) lower than 30 mK at room temperature. The full frame dimensions are 640 x 480 pixels and the corresponding sampling frequency is 30 Hz. The thermograms are transferred to a PC via FLIR ExaminIR software thanks to a firewire connection. Figure 4.1 shows the components of the system setup.

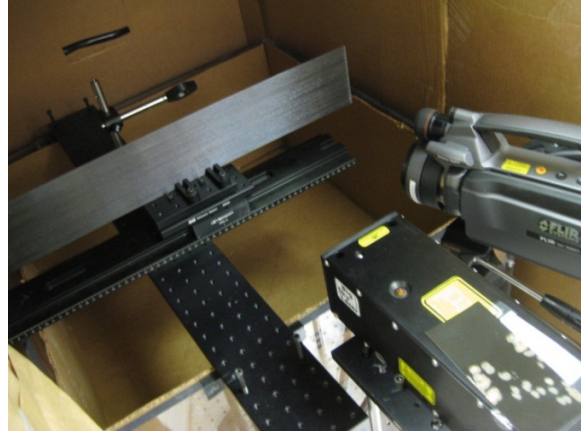


Figure 4.1. Experimental setup: marked horizontal guide, composite plate, laser source, infrared camera, cardboard box.

The distance between the camera and the test specimen was approximately 300 mm, the minimum required for a well focused image according to the objective mounted on the camera (see the FLIR User's manual [25]).

Despite the dark surfaces, the specimens present lightly reflective faces. Radiations from the surroundings can hit these reflective planes and reach the infrared device altering the temperature measure. Thus, the entire system setup is enclosed by a big cardboard box to screen the infrared radiation from possible external sources. Moreover, to measure temperature accurately the following object parameters must be set: emissivity, reflected temperature, humidity and atmosphere temperature. The most important is the emissivity value that represents a measure of how much radiation is emitted from the object, compared to that from a perfect blackbody at the same temperature:

$$\varepsilon = \frac{W_{object}}{W_{blackbody}} \quad (4.1)$$

where W is the radiation power measured in Watt/m^2 according to the Stefan-Boltzmann's law:

$$W_{blackbody} = \sigma T^4 \quad (4.2)$$

T stands for the temperature of the black body and σ is a constant value equal to $5.67 \cdot 10^{-8} \text{ Watt/ (m}^2 \text{ K}^4)$. The higher the temperature, the more the power emitted. The camera output signal mostly depends on the emissivity value. In particular, for the temperature measure, the infrared device takes into account three terms: radiation emitted from the object, radiation from the surrounding reflected by the object and radiation emitted from the atmosphere. If the specimen is well screened, the last two terms can be neglected. Then the output signal can be approximated as:

$$U = C \varepsilon W_{blackbody} \quad (4.3)$$

where C is a constant.

Ideally, the emissivity can assume values between 0 and 1 and it is a function of the temperature (see Equation 4.1 and Equation 4.2). Normally, object materials and surface treatments exhibit emissivity ranging from approximately 0.1 to 0.95. A highly polished (mirror) surface falls below 0.1, while an oxidized or painted surface has a higher emissivity. (Human skin exhibits an emissivity 0.97 to 0.98).

Non-oxidized metals represent an extreme case of perfect opacity and high reflexivity, which does not vary greatly with wavelength. Consequently, the emissivity of metals is low, only increasing with temperature. For non-metals, emissivity tends to be high, and decreases with temperature.

4.2.2 First study: unidirectional CFRP plate, detection of surface cracks

The analysis presented here refers to the unidirectional carbon fibre plate. Surface damages were created by means of a cutter performing four cracks of a width gap and a depth of approximately 0.5 mm. The length of these cracks varied from 4 to 150 mm. In total there are 16 scanning points, the first eight associated with pristine areas and the last eight associated with damaged areas. Figure 4.2 schematizes the defects on the surface of the plate and the scanning point locations (representation not in scale).

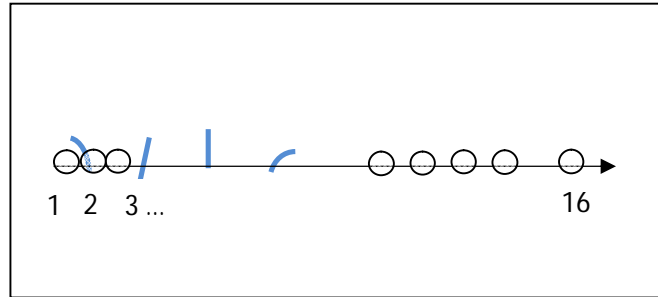


Figure 4.2. Schematization of the defects (blue color) and the scanning points (transparent circles) for the first experiment.

Observing the instructions reported in Table 4.1, the object and acquisition parameters are set as follow:

Table 4.2. Object parameters and acquisition features set for the first experiment

Object parameters	
Reflected temperature [°C]	23
Emissivity	0.86
Humidity	50%
Distance [m]	0.3
Atmosphere temperature [°C]	23

Acquisition parameters	
Acquisition time [s]	5
Frame rate [Hz]	30
Window size [pixel x pixel]	640x480

Following the procedure explained in the previous section, a baseline video is created by averaging the acquisitions associated with the eight pristine regions of the sample to reduce the effect of thermal noise. For each scanning point the mean temperature, variance, skewness, and kurtosis of the frames are computed. Figure 4.3 shows these features as a function of the frame number for an acquisition associated with a pristine zone.

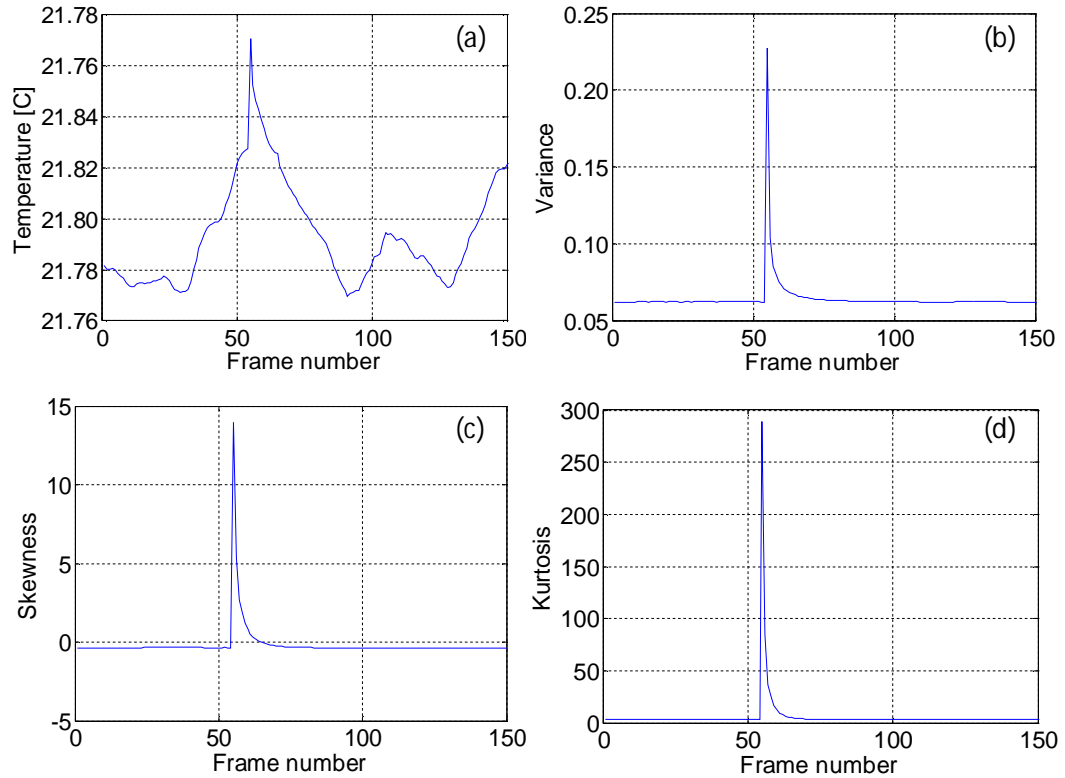


Figure 4.3. (a) Average temperature, (b) variance, (c) skewness, (d) kurtosis of the ROI of the video sequence associated with one of the pristine areas of the test specimen.

When compared to the average temperature, which is a parameter widely used in active and passive thermographic methods, the three statistical parameters denote a much sharper increase immediately after the laser pulse.

They are used to identify the frame of the sequence taken immediately after the release of the laser beam.

In particular, the skewness measures the asymmetry of a data set around the data mean and it is compute as:

$$y = \frac{1}{N} \frac{\sum_{i=1}^N (x_i - \bar{x})^3}{\sigma^3} \quad (4.4)$$

where N is the number of elements of the distribution \bar{x} is the mean and σ the estimated standard deviation [26].

Negative values represent data that are skewed leftward with respect to the mean. Positive values represent data that are skewed rightward, as it happen in all the laser spot thermography tests for the local increase of temperature. The skewness coefficient of the normal distribution (or any perfectly symmetric distribution) is zero. Thus, positive skewness values are expected.

The kurtosis is a measure of how outlier-prone a distribution is and it is defined as:

$$k = \frac{1}{N} \frac{\sum_{i=1}^N (x_i - \bar{x})^4}{\sigma^4} - 3 \quad (4.5)$$

The kurtosis of the normal distribution is equal to three. Distributions that are less outlier-prone have kurtosis lower than three. Conversely, distributions that are more outlier-prone than the normal distribution have kurtosis greater than three, as the present situation has.

For each scanning point, the frame with the largest skewness and kurtosis is picked and processed by using the two-stage algorithm proposed. Figure 4.4 presents images from four ROIs of 90 x 90 pixels, covering an area of 625 mm².

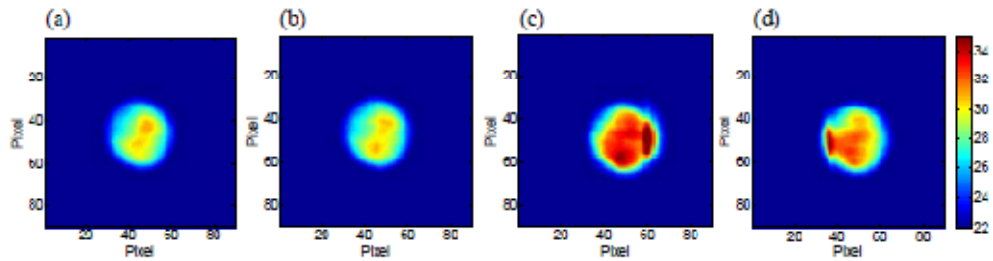


Figure 4.4. Thermal images of four scanned points. (a, b) Undamaged areas. (c, d) Damaged areas. All images had the highest kurtosis and skewness of their respective sequence.

Figure 4.4a and Figure 4.4b are recorded from sound regions, whereas Figure 4.4c and Figure 4.4d. are associated with two damage cases. The overall temperature of the damage cases is higher. The temperature difference is largely due to the presence of the defect that entraps heat and partially due to time gap between the laser shot and the infrared snapshot.

Figure 4.5a shows the correlation coefficient associated with the 16 scanning points.

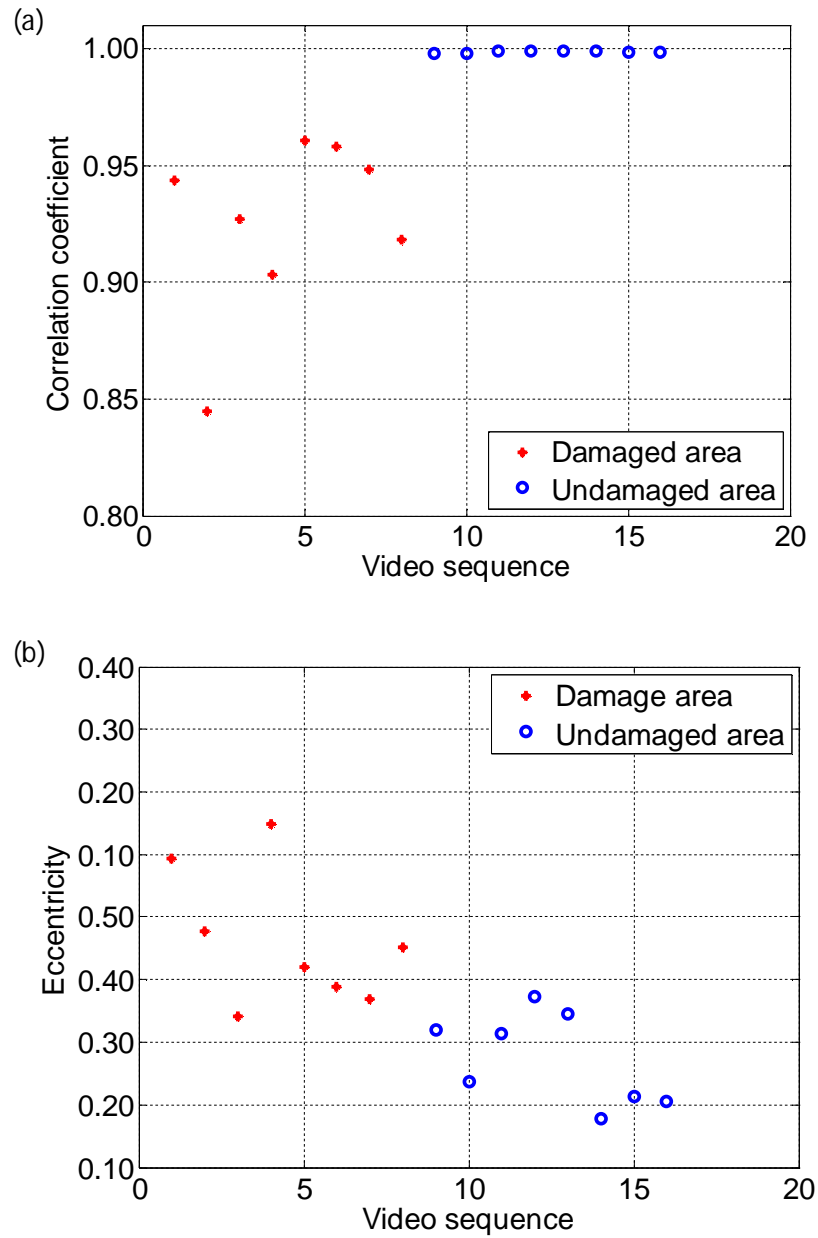


Figure 4.5. (a) Correlation coefficient and (b) eccentricity associated with the 16 scanned points for the test object of the first experiment.

All 16 frames are compared to the baseline frame. The first eight points refer to damaged areas. A clear step between damaged and undamaged cases is visible and it is possible to set a threshold level for instance at 0,980. Correlation coefficients that fall below the threshold, warn about the possible presence of a defect. Figure 4.5*b* shows the eccentricity as a function of the scanning point. The discrimination between the two structural states is not as evident as in Figure 4.5*a*. Moreover, the eccentricity of the sound regions is expected to be close to zero. The reason for such a discrepancy is two-fold. First, the laser spot is not perfectly circular probably due to the optics of the laser. Second, the directionality of the fibers implies that the thermal conductivity of the specimen is not homogeneous. Such the thermal flow has a directional pattern. Nonetheless, the proposed algorithm should not be impaired as it relies on the comparison between testing and baseline images.

Figure 4.6 displays the absolute first and second derivatives of the temperature relative to the four structural conditions in Figure 4.4.

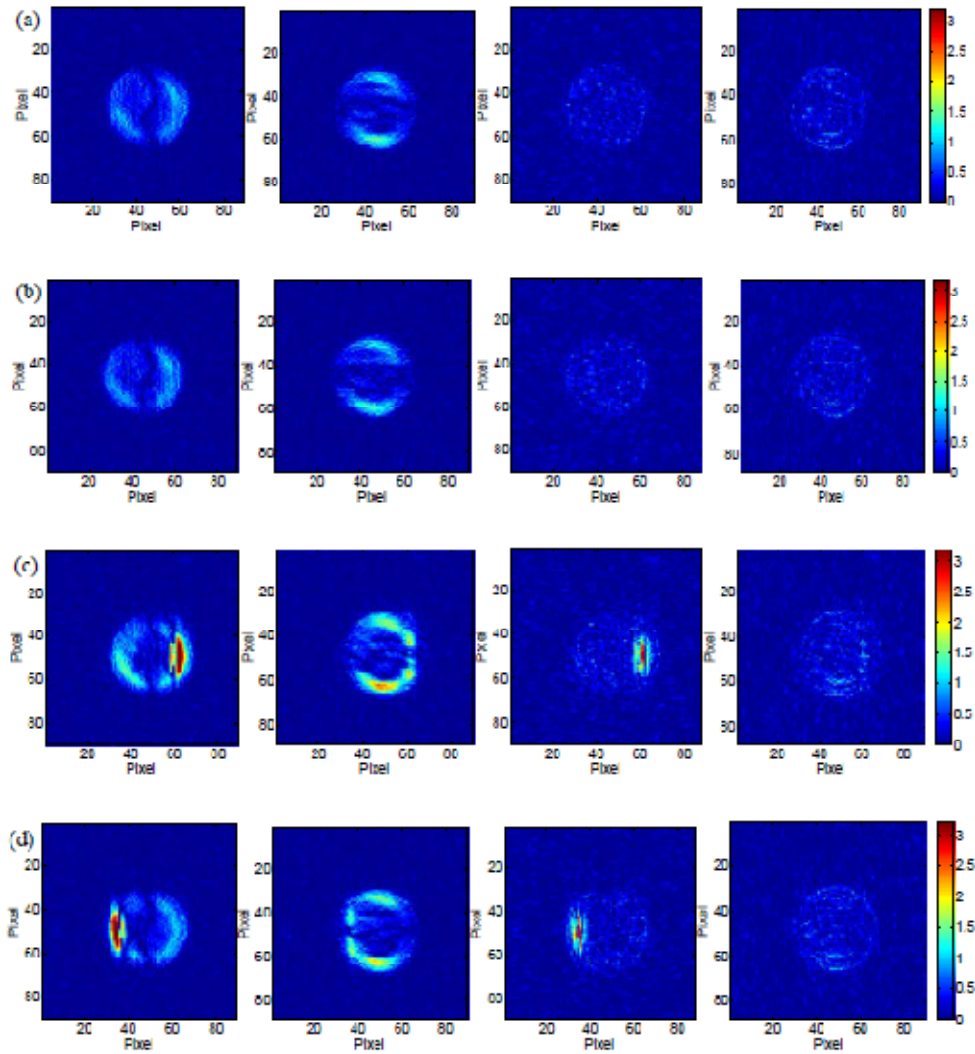


Figure 4.6. Absolute first derivative along x (leftmost column) and along y (second column). Absolute second derivative along x (third column) and along y (rightmost column). (a) Scanning point 10 (no damage). (b) Scanning point 11 (no damage). (c) Scanning point 2 (damage). (d) Scanning point 3 (damage).

While the first derivative produces false positives around the circular edge of the spot, the second derivative clearly highlights the presence of the vertical cracks.

Figure 4.7 shows the results of the Laplacian and Roberts filters applied to the frames presented in Figure 4.4.

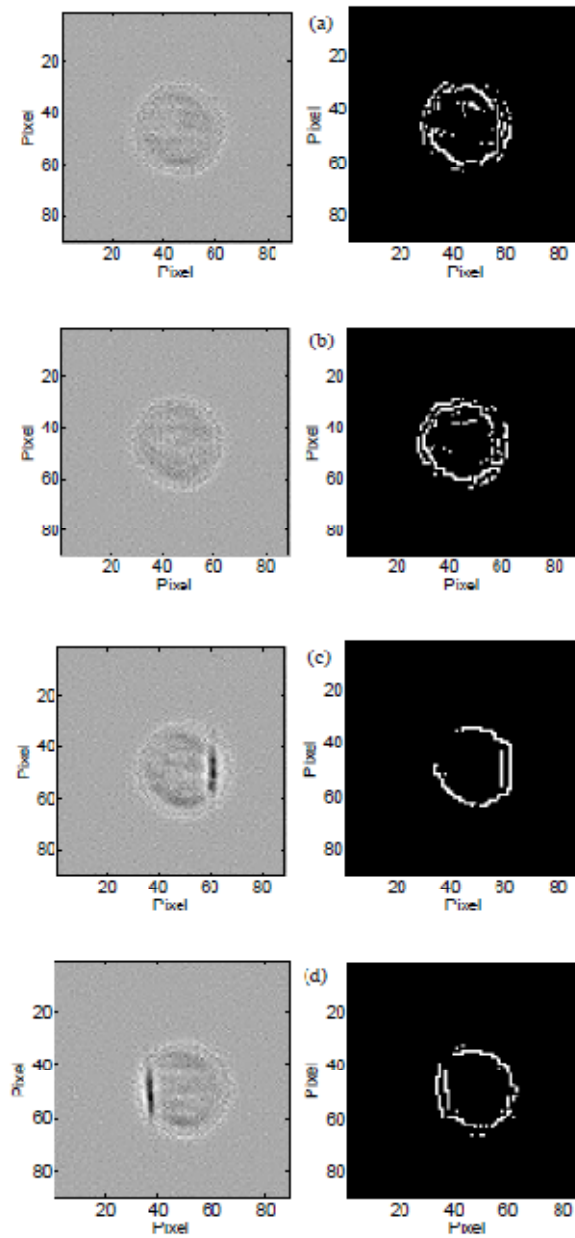


Figure 4.7. Thermal image after the application of the Laplacian filter (left column) and Roberts filter (right column). (a) Scanning point 10 (no damage). (b) Scanning point 11 (no damage). (c) Scanning point 2 (damage). (d) Scanning point 3 (damage).

Both identify properly the location of the crack. Overall, the application of the Laplacian filter outperforms the Roberts filter, although the latter seems to better isolate the contour of the defect.

4.2.3 Second study: unidirectional CFRP plate, detection of impact damage

In the present section, the same carbon fiber composite plate is inspected, but the region scanned (an area of approximately 110 x 80 mm) is different. Impact-related damage of almost 25 J was induced by means of a falling weight. The plate results visibly compromised for an area of about 1 cm².

Thirty-seven acquisitions are recorded: nineteen for the first row and eighteen for the second. The spatial increment between each scanning point is 0.5 mm with a little overlap of the spots not to lose information. A sketch showing the scanning process is provided in Figure 4.8.

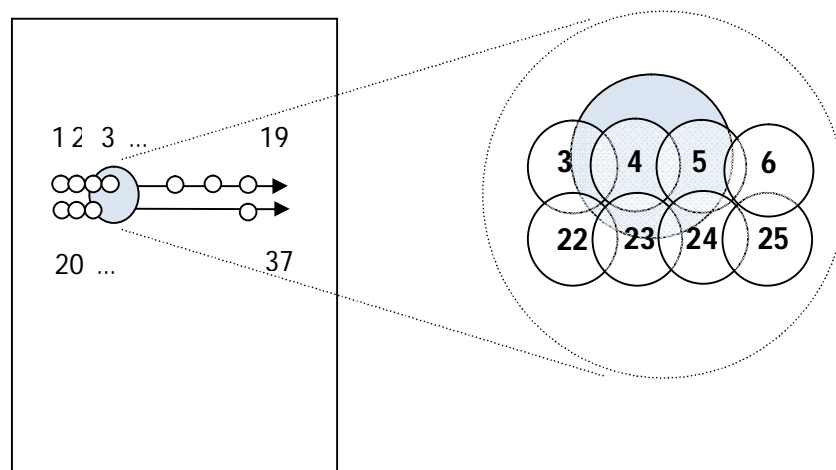


Figure 4.8. Schematization of the scanning points for the second experiment and zoom of the damaged area.

Acquisitions marked as suspected are expected to be found between the third and the fifth scanning point and between the 22nd and the 25th point.

The object parameters are the same as the first experiment (see Table 4.2). The acquisition parameters, instead, are:

Table 4.3. Acquisition parameters for the second experiment

Acquisition parameters	
Acquisition time [s]	3
Frame rate [Hz]	120
Window size [pixel x pixel]	640x60

While using a reduced window size (640 x 60 rather than 640 x 480 pixels), it is possible to exploit a higher frame rate. The aim is to verify whether a higher sampling frequency yields more accurate temperature measurements as soon as the laser beam is released. Unfortunately, the laser shot and the sampling frame rate are not synchronized and this introduces problems while seeking for the *first shot frame*. The peaks in the average temperature, standard deviation, skewness and kurtosis graphs do not occur always in correspondence of same frame. Thus, there is not a unique estimation of the instant of the laser fire. Due to the bad synchronization between the laser pulse and the camera sampling time, some thermograms present a smaller or distorted hot spot; some other a well expanded hot circle. Figure 4.9 shows the phenomenon.

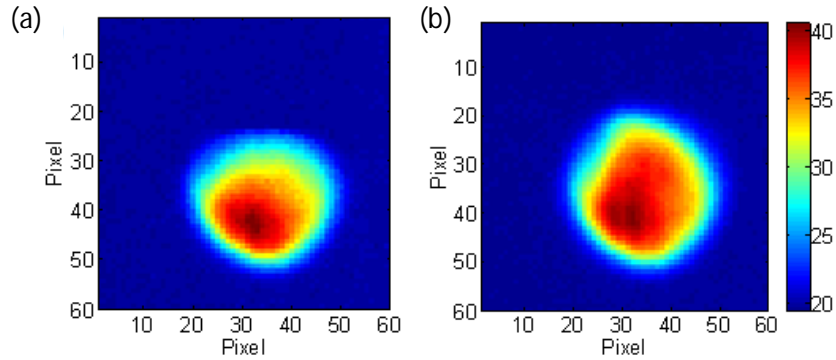


Figure 4.9. The problem of synchronization. Two consecutive frames of acquisition number 6 regarding a pristine area: (a) Frame 297 identified as first shot frame by skewness and kurtosis parameters; (b) Frame 298 identified as first shot frame by average temperature and variance parameters.

For the same video sequence, the average temperature graph and the variance graph present peaks in correspondence of the frame 297, skewness and the kurtosis graph in correspondence of the frame 298. Since the last two parameters can measure the outlier values in a distribution, it seems more reasonable to select the frame pointed out by these two statistical values as the instant of the excitation start (frame 298 in this case).

Once the first shot frame is picked, the thermal image is process. The region of interest in this case is 60 x 60 pixels. Figure 4.10 shows the first shot frame for the recreated baseline data sequence (see step 4 of the algorithm previously discussed).

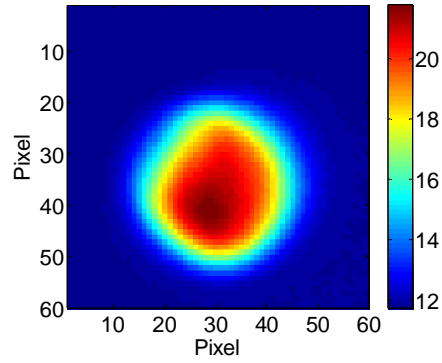
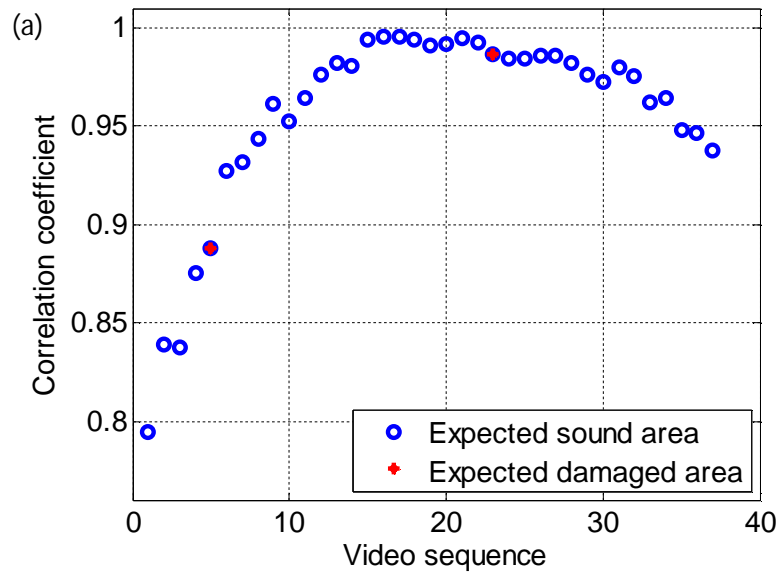


Figure 4.10. *First shot frame* for the recreated baseline video.

Each acquisition is compared to the frame above (Figure 4.10). Figure 4.11 presents the correlation coefficients for each scanning point.



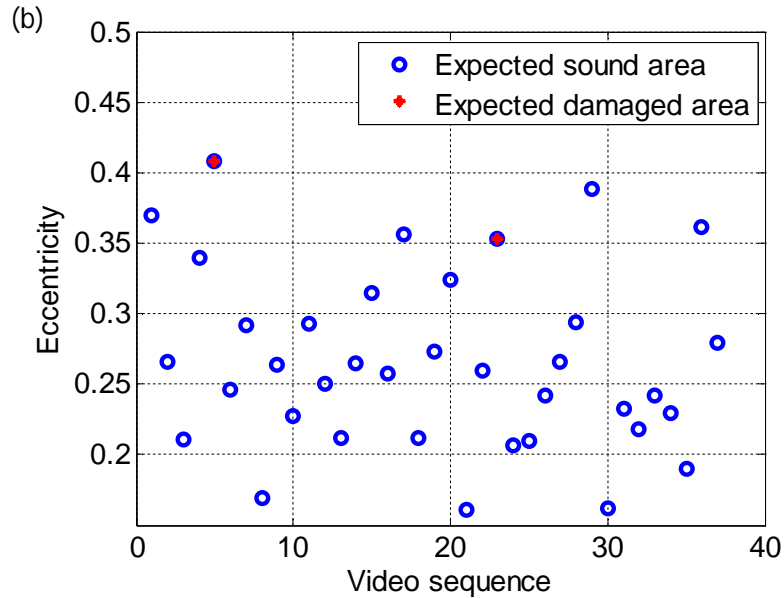


Figure 4.11. (a) Correlation coefficient and (b) eccentricity associated with the 37 scanned points for the test object of the second experiment.

Acquisitions corresponding to the scanning point 5 and scanning point 23 can be considered suspicious since they present high eccentricity value and low correlation (especially acquisition number 5). However, these parameters do not stand out clearly from the ones regarding the sound areas. No threshold values can be defined. This fact compromises the reliability of the algorithm. For example, inspection point 29 can be considered as a false positive acquisition. It presents an eccentricity higher and a correlation coefficient lower than point 23 (damage case), but it is known to concern to a pristine area around 2 cm far from the damage. The image enhancement, though, can help in certain situation in visualize the defect. Figure 4.12 shows four different scanning points: two undamaged situations on the left and two damage situations on the right.

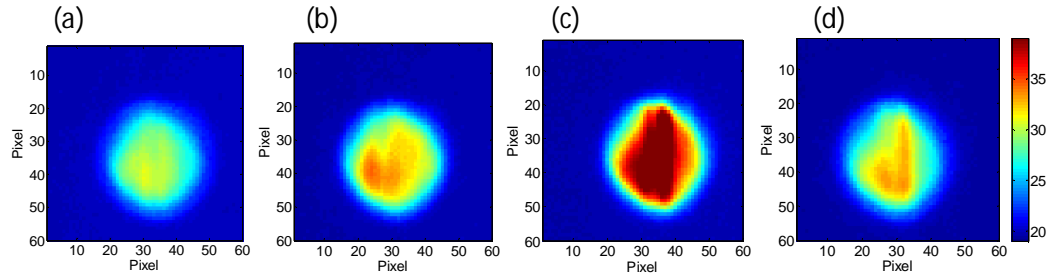


Figure 4.12. Thermal images of four scanned points. (a, b) Undamaged areas. (c, d) Damaged areas. All images had the highest kurtosis and skewness of their respective sequence.

The heat is entrapped and a local increase of temperature is remarked by the thermal image corresponding to point 5 (see Figure 4.12c). For scanning point 23 this is not so appreciable. The same situation occurs while computing the first and second derivatives: the temperature gradient presents outstanding values in correspondence of the edges of the defect for acquisition 5 but not for acquisition 23. Figure 4.13 illustrates the above. (Image processing for pristine areas are here omitted since it yields results similar to the one proposed in the previous study, see Figure 4.6a,b and Figure 4.7a,b).

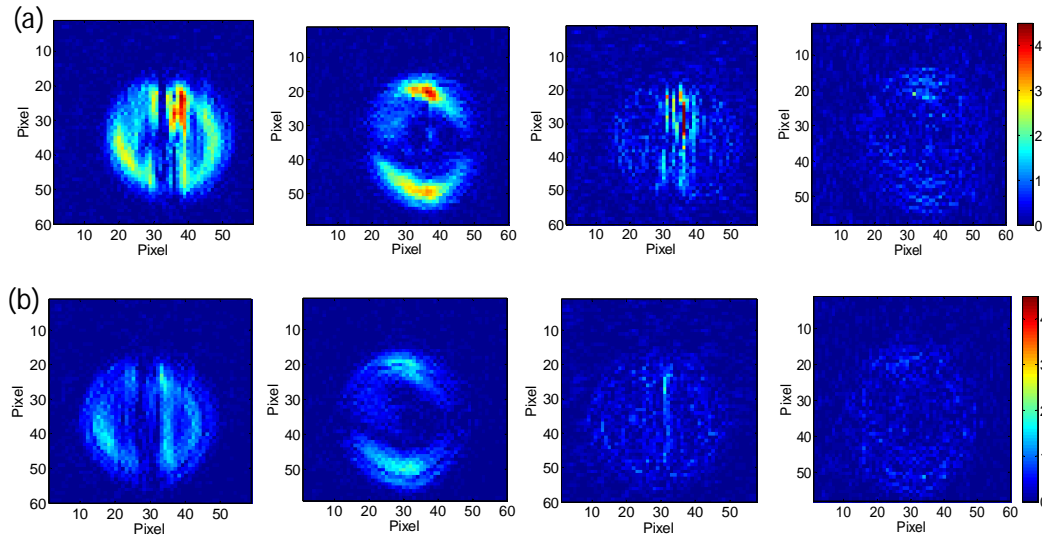


Figure 4.13. Absolute first derivative along x (leftmost column) and along y (second column). Absolute second derivative along x (third column) and along y (rightmost column). (a) Scanning point 5 (damage). (b) Scanning point 23 (damage).

The impact of the falling mass creates a crushing of fiber in the composite plate, and in extremely cases, it can generate tears along the fiber direction. Between the tear faces, the heat can be entrapped due to the low conductivity of the air. Video sequence 5 represents this situation. The red vertical lines correspond to the heat accumulation between the fibers. When the impact causes just a compression of the layers of the composite material, the heat is able to flow into the specimen without abrupt discontinuities. Video sequence 23 represents this scenario. The laser beam hits the compromised area but in correspondence of the notch and not of the crack, so that, the damage is not easily recognized. No false positives occur in this image processing in the second derivative images.

Laplacian filter reacts same way as the thermal gradients, revealing the edges for scanning point 5 but not for scanning point 23. Roberts seems to be the most helpful

procedure since it shows a clearly distorted circular spot. The vertical lines lie right in correspondence of the tears present in the specimen.

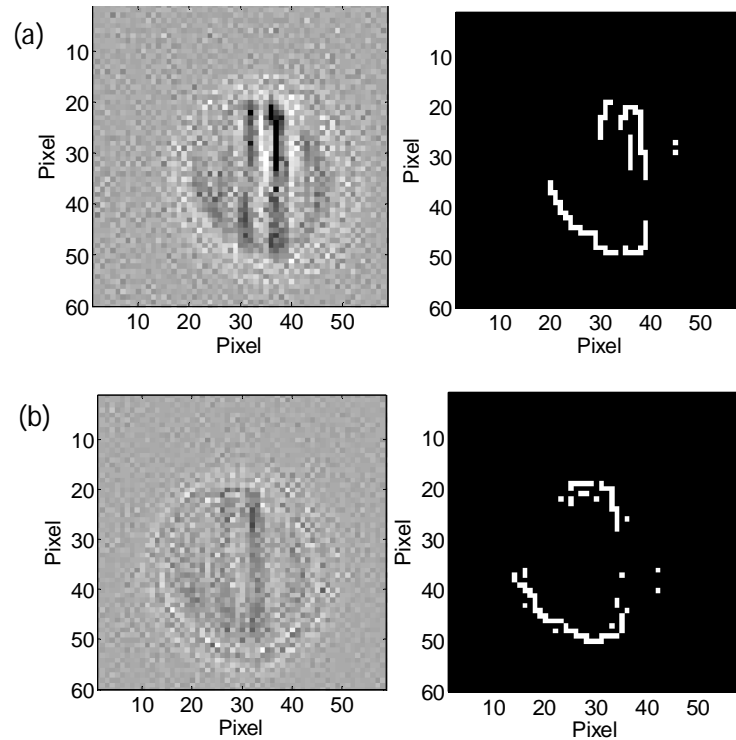


Figure 4.14. Thermal image after the application of the Laplacian filter (left column) and Roberts filter (right column). (a) Scanning point 5(damage). (b) Scanning point 23 (damage).

It is possible to conclude that for the impact damage the algorithm is not reliable at all. The mathematical and statistical parameters can help in the evaluation of the damaged area but some false positive values can occur. The image enhancement based on the estimation of the first and second derivative and on the Laplacian filter can fail in detecting the defect boundary when it concerns only a crushing of fibers. Better results can be obtained by the application of the Roberts filter.

4.2.4 Third study: bidirectional GFRP plate, detection of different damages

Glass fiber reinforced composite materials are widely used in the production of aerospace structures. Several quality controls are required. In this section, a surface breaking crack and three impact related damages are realized. The crack is performed by means of a little milling cutter and it presents a gap and a depth of 1 mm, a length of 10 mm approximately. The other three damages are performed by mean of a falling weight that impacts perpendicular onto the surface of the composite plate. The impact energy is approximately 10 J for the first impact (*Impact 1*, see Figure 4.15) and 25 J for the second and the third (*Impact 2 and Impact 3*). Each impact yields a damaged zone of about 1 cm².

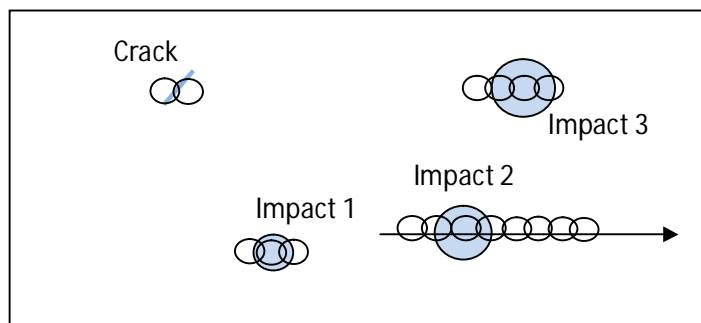


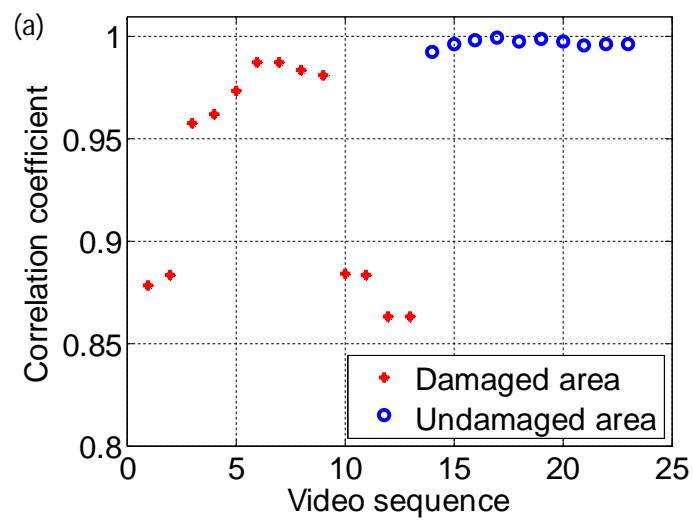
Figure 4.15. Schematization of the defects and the scanning point positions for the third experiment.

In total, there are 23 data sequences, in particular: 13 inspections in proximity of defects and 10 baseline inspections.

The object and the acquisition parameters are the same as the previous experiment (see Table 4.2 and Table 4.3. Acquisition parameters for the second experiment). Due to the high frame rate, synchronization problems come out as explained in the second study. The *first shot frame* to be compared to the baseline-recreated video

and to be processed according to the algorithm thus far discussed, is flagged by the maximum value of the kurtosis coefficient.

Figure 4.16 presents the results for the computation of the correlation coefficient and the eccentricity values.



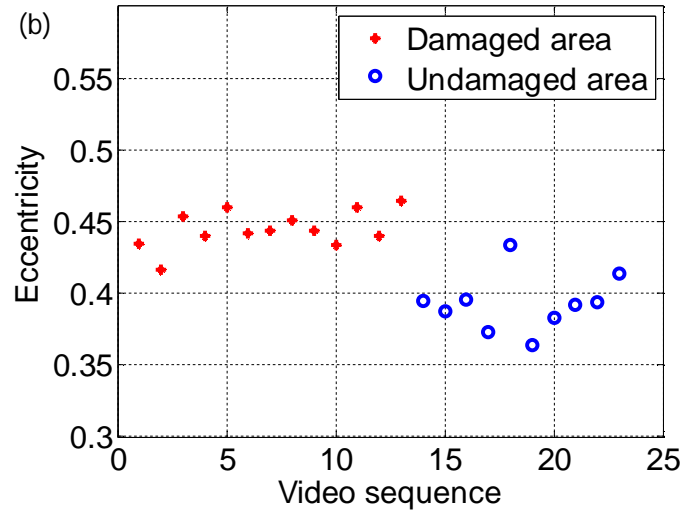


Figure 4.16. (a) Correlation coefficient and (b) eccentricity associated with the 23 scanned points of the test object of the third experiment.

Video sequence 1 and 2 regard two laser pulses respectively addressed to the left and to the right side of the crack. The cut is clearly pointed out thanks to correlation values that fall below 0,900 (respectively 0,878 and 0,883) and to an eccentricity higher than 0,415. Acquisition 3, 4 and 5 regard the scanning points around the first impact damage. Correlation coefficients are still under a threshold level settable at 0.988. Eccentricity is higher than the value for the crack situation. The same situation occurs for the second impact (acquisitions 6, 7, 8 and 9) even if the correlation coefficients lie closer to the threshold. The best scenario regards the third impact damage (points 10 to 13), which presents on average the lowest correlation coefficients (0,863 for video sequence 12) and the highest eccentricity values (0,4646 for acquisition 13).

Thus far, the results for the present experiment are very promising since allow the operator to identify damaged areas automatically without observing each frame acquired. And this is one of the main goals of the present work.

In contrast with the studies reported in the last sections, for this type of material the image enhancement procedure turns out not to be helpful in visualizing the defect neither for the crack nor for the impact related damages. Figure 4.17 presents a thermogram for a pristine zone and a thermogram for the damaged area. Figure 4.18 the thermal gradients computed in both directions vertical and horizontal.

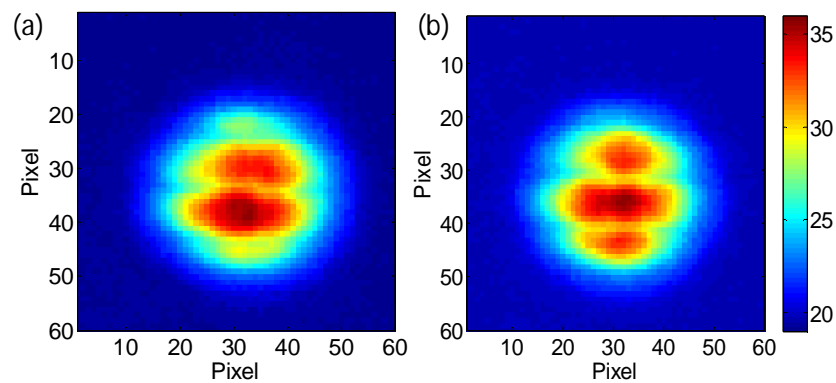


Figure 4.17. Thermal images of two scanned points. (a) Undamaged area (video sequence 21). (b) Damaged area (video sequence 8). All images had the highest kurtosis and skewness of their respective sequence.

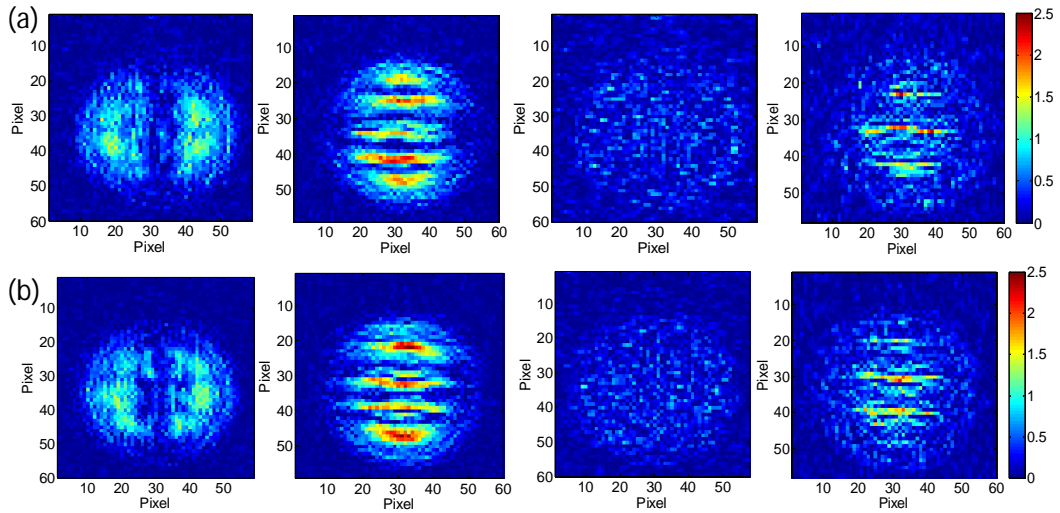


Figure 4.18. Absolute first derivative along x (leftmost column) and along y (second column). Absolute second derivative along x (third column) and along y (rightmost column). (a) Scanning point 21(no damage). (b) Scanning point 8 (damage).

The heat generated by the laser flows rapidly into the specimen along the fibers revealing the reticular structure of the plate. Horizontal stripes are evident in the thermal images suggesting the direction of the fiber in the upper layer. Vertical stripes are a little less visible. This preferential pattern for the heat propagation probably hides the distortion expected for the presence of the defect. Figure 4.19 provides the results of the application of the Laplacian and the Roberts filter.

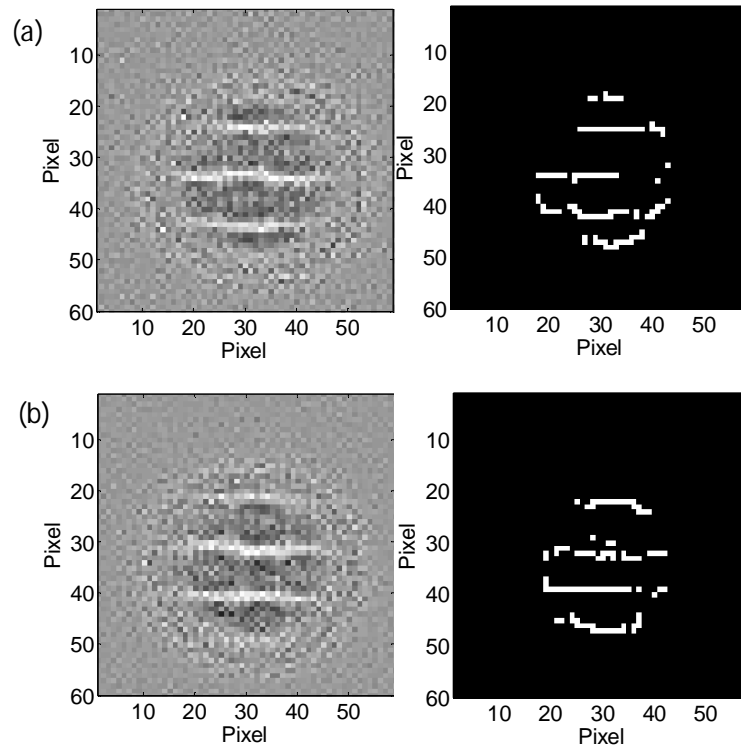


Figure 4.19. Thermal image after the application of the Laplacian filter (left column) and Roberts filter (right column). (a) Scanning point 21 (no damage). (b) Scanning point 8 (damage).

The 90° fiber layers stand out in the circular area heated by the laser beam. Roberts filter keep only the horizontal lines designing the direction of the fiber on the sample surface.

4.3 Tensile test experiments

The tensile fracture behavior of a dual phase high performance steel is investigated here with the aid of the infrared thermography.

The infrared camera is employed for in-situ monitoring of progressive damages of the samples during monotonic loadings. In particular, the exploited NDE technique is used to facilitate a better understanding of damage evolution in tensile testing.

4.3.1 System setup

The testing material used for this investigation is a dual phase high performance steel. Dual phase steel (DPS) features a (soft) ferrite microstructure, with a matrix containing islands of martensite (increasing the tensile strength) in the secondary phase (with proportional volume fraction increase in analogue to tensile strength). Figure 4.20 presents a schematic view of the production process and the resulting material microstructure.

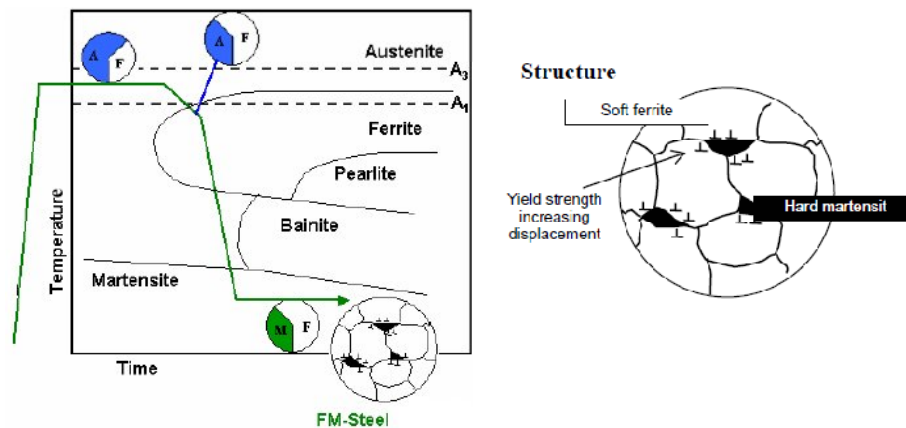


Figure 4.20. Production process (left) and microstructure scheme (right) for a DPS

Dual-phase steel presents a low yield to tensile strength ratio, high tensile strength, work hardening rate and strain rate sensitivity (the faster it is crushed the more energy it absorbs), and good fatigue resistance. Due to these properties, DPS is often used for automotive industry, especially for body panels, wheels, and bumpers.

Figure 4.21 presents the standardized geometry of the testing samples and their range of chemical composition in weight percentage.

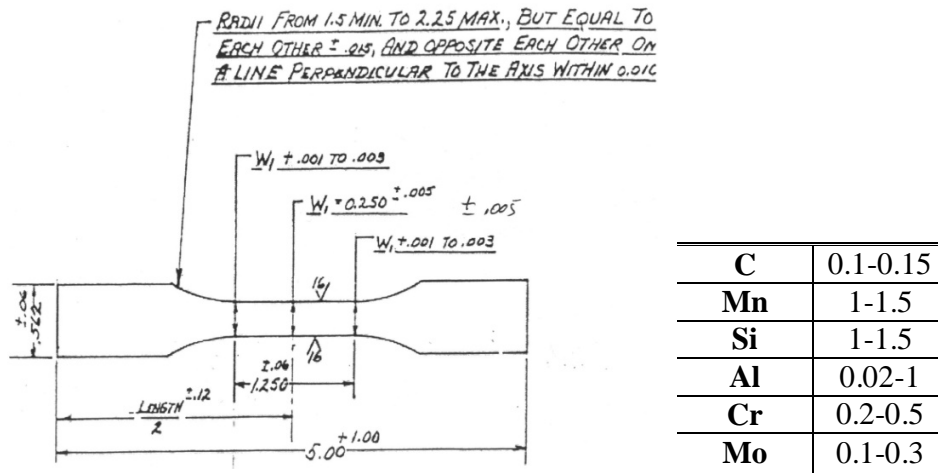


Figure 4.21. The tensile coupon of high performance steel. The drawing of sample dimensions and the chemical composition.

During the test, the specimen is grabbed by the two grips of the tensile testing machine. The IR camera is addressed to the sample and used to monitor surface temperature changes. It is connected through a firewire cable to a PC in order to record and save the image sequences. The high frame rate guarantees instant image capture during tensile testing. Figure 4.22 illustrates the principal components of the system setup.

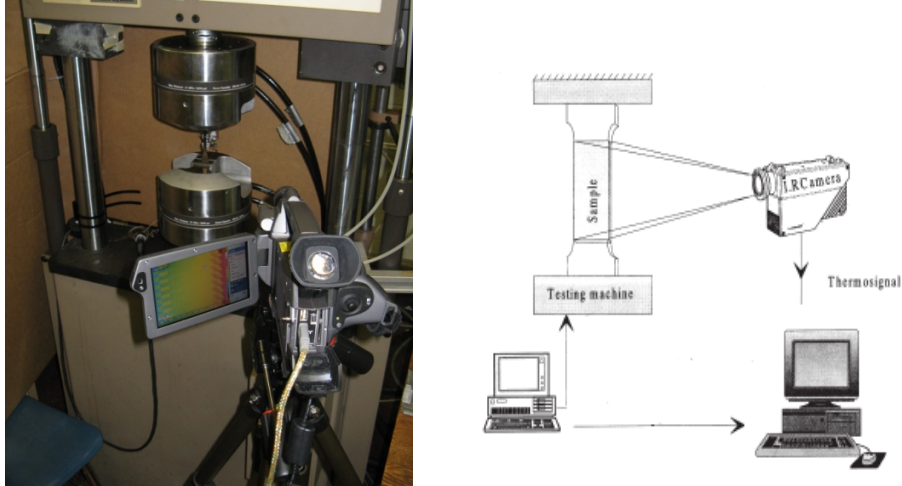


Figure 4.22. Picture and schematization of the experimental setup: tensile testing machine, infrared camera, and connected control units.

A secondary computer is connected to the tensile testing machine. The experiments are conducted under displacement control at a crosshead speed of 4 mm per minute at room temperature until fracture. The specimens fail around the second minute of stimulation. Data about the stress and the elongation of the sample are recorded and compared to the camera data outputs. The results of the analysis and the image processing for this study are reported in the next section.

4.3.2 Tensile testing results

Thanks to the data collected through the tensile machine control, it is possible to draw the characteristic curve of the material. Figure 4.23 presents the tensile stress trend as a function of the strain and of the time of the DPS specimen.

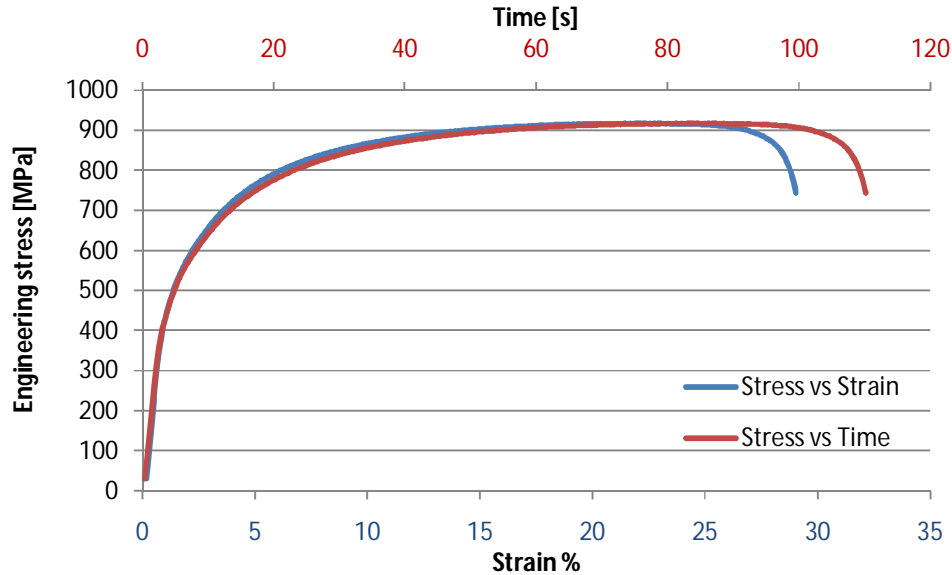


Figure 4.23. Stress-strain curve (blue line) and stress trend as a function of time (red line).

The tensile failure behavior shows an initial elastic region for the first couple of seconds, a yielding stress at around 450 MPa, a continual stress increase before reaching ultimate tensile stress (UTS) equal to 900 MPa after around 90 seconds of loading and finally a gradual stress decrease until final failure. The failure occurs after 110 seconds. The mechanical behavior, described by the curves of Figure 4.23, is coupled to the thermal trend reconstructed through the infrared data acquired. For the recording of the thermograms, the object and the acquisition parameters are set on the IR camera as Table 4.4 shows.

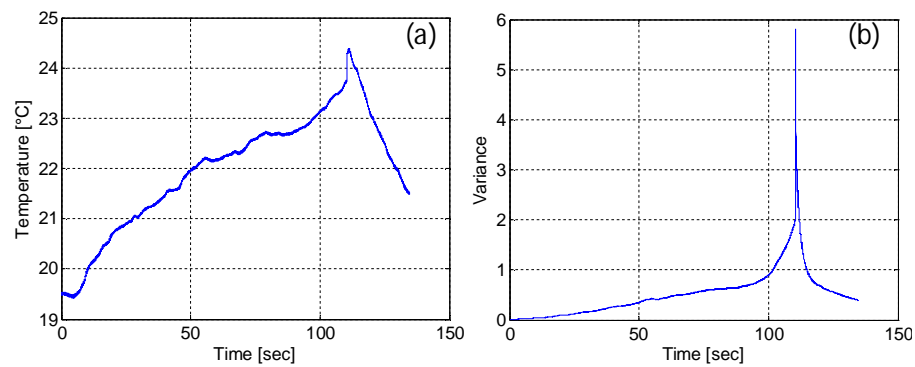
Table 4.4. Object and acquisition parameters for the second experiment

Object parameters	
Reflected temperature [°C]	23
Emissivity	0.65

Humidity	50%
Distance [m]	1
Atmosphere temperature [°C]	23

Acquisition parameters	
Acquisition time [min]	3
Frame rate [Hz]	120
Window size [pixel x pixel]	640x60

For this kind of test, the image processing algorithm has been slightly modified. The eccentricity value is no more computed since no circular hot spots are expected. The statistical parameters are calculated now in order to flag the instant of the sample failure. Figure 4.24 presents average temperature, skewness and kurtosis trend for the considered DPS sample.



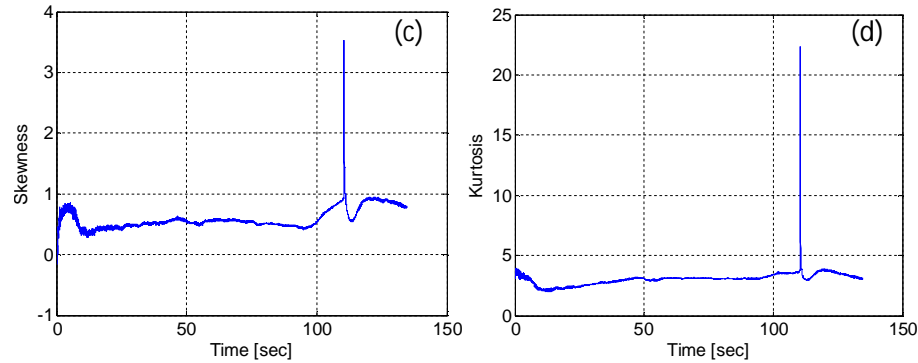


Figure 4.24. (a) Average temperature, (b) variance, (c) skewness, (d) kurtosis of the ROI from the video sequence regarding a DPS sample .

In the graphs above, outlier values create spikes exactly in correspondence of the breaking instant of the tested sample (second 110.3) according to the stress-strain curve (see Figure 4.23). As explained in the first chapter, the work done to the system by plastic deformation is identified as the major contribution to heat effect. Passing the time the sample section interested by the plastic deformation increases and thus, the energy dissipation let the specimen temperature augments (see Figure 4.24a). The highest value is recorded for the last frame before failure. Once the sample fails, the tensile machine stops working and no more displacement is applied to the sample. The failure extremities rapidly cool down and the temperature trend presents a negative slope. The instants right before the breaking correspond to moments of high concentration of stress. The material microstructure is changing and the friction between the crystalline planes causes part of the dissipated energy. The largest values for the variance, skewness and kurtosis are related to these moments.

The correlation coefficient is computed, as usual, comparing each frame of the video sequence to a reconstructed reference frame evaluated by averaging more

than 200 frames acquired before the displacement application. Figure 4.25 shows the correlation coefficient trend overlapped to the stress trend, both as function of the time.

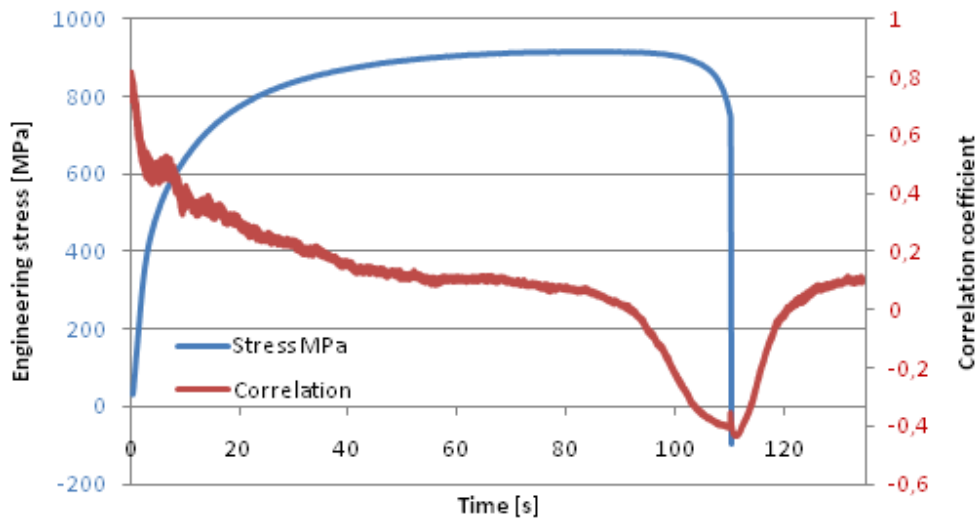


Figure 4.25. Engineering stress trend (blue line) and correlation coefficient trend (red line) as a function of the time.

The results from this diagram are quite promising. Since the temperature in the sample increases, the correlation to the reference frame assumes values smaller and smaller. In correspondence of the failure a little spike appears. Then, the displacement is stopped and the sample regains the initial elastic elongation. The cooling down starts; the sample reaches the thermal equilibrium with the room temperature as the initial condition. The correlation coefficient presents a positive slope.

In detail, it is possible to divide the area of the diagram in Figure 4.25 into four regions (neglecting the data after the fracture) and to approximate the correlation-time curves with linear segments connected each other at the subdivision

boundaries. Every change in the slope of a segment corresponds to the transition from a particular state to another.

Figure 4.26 illustrates the above.

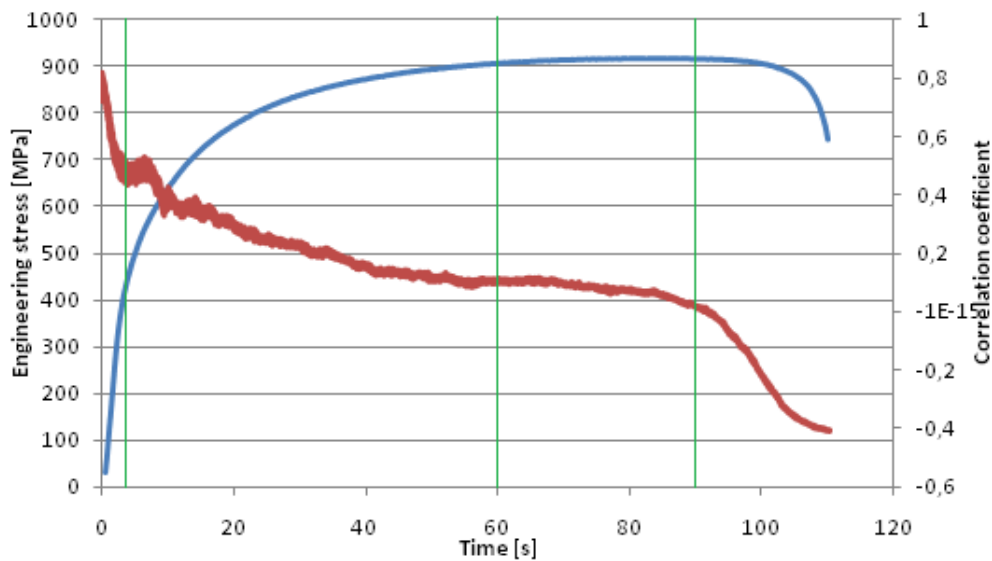


Figure 4.26. Four subdivisions for the correlation coefficient trend compared to four changes in the sample response to the displacement.

The first zone regards the elastic deformation: the segments approximating the stress-time and the correlation trends present a negative high slope. The slope decreases in the second region regarding the yielding and the hardening phase, remaining negative. Then, a plateau suggests a stationary condition of the sample: no increase in stress, no temperature increase and consequently no correlation decrease. The last subdivision corresponds to the necking of the sample when the engineering stress tends to fall down and the correlation coefficient cross the zero level to reach larger and larger negative values until failure. The results are quite

promising since the correlation coefficient seems to describe well the stress trend in the specimen. This has been proven also for other four tests on similar DPS samples. The fracture in these experiments is easily visible at naked eye. The evaluation of the thermal gradients and the application of the spatial filtering do not intent to detect the defect but can be exploited to visualize the temperature evolution passing the time. Figure 4.27 reports thermograms grabbed at three different consequential instants (named afterwards *hot spot*, *heat column* and *fracture*). The region of interest regards only the gauge section.

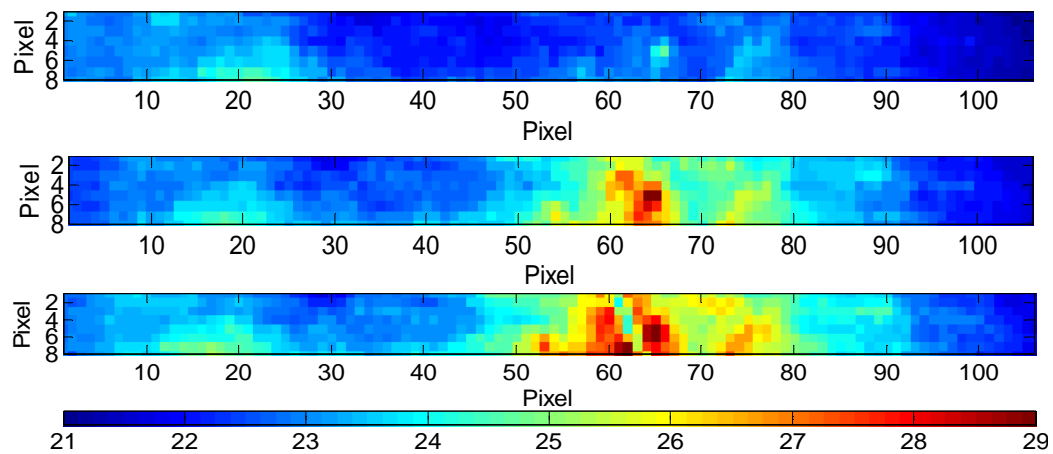


Figure 4.27. Temperature distribution on the sample surface at three different consequential instants (respectively top to bottom). The color bar indicates the temperature range [°C].

A hot spot appears right in the mid section of the sample (pixel coordinates (4,67)) after several seconds of elongation (around the 90th second). Then, the stress in the specimen increases realizing a heat column running along the width of the sample and getting more and more visible until few seconds before the failure. Once the sample fails, the fracture faces depart from each other and start to cool down.

An increase of temperature occurs also at the bottom left side of the sample. This is believed to be due to the misalignment of the sample. Alignment of the test specimen in the testing machine is critical, because if the specimen is misaligned, either at an angle or offset to one side, the machine exerts a bending force on the specimen. The flexional stress component is pointed out by the infrared camera.

The qualitative image processing, regarding the second stage of the discussed algorithm, helps in visualize the evolution of the heat passing the time.

Figure 4.28, Figure 4.29 and Figure 4.30 present the absolute derivatives in both directions x and y and the results of the application of the Laplacian and Roberts filter for the three thermograms.

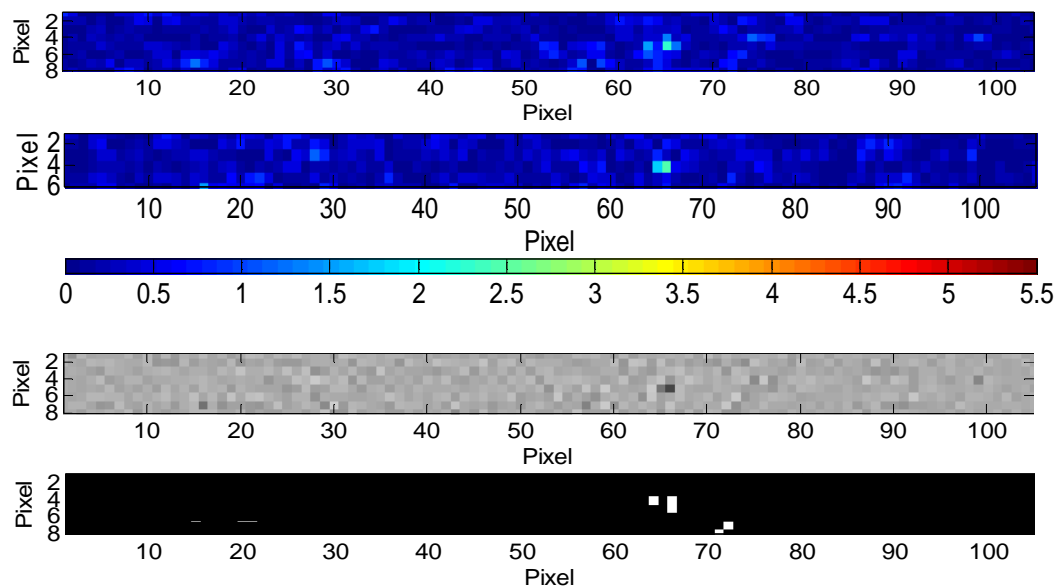


Figure 4.28. Hot spot. (Top to bottom). Absolute second derivative in x direction and in y direction. Laplacian and Roberts filter.

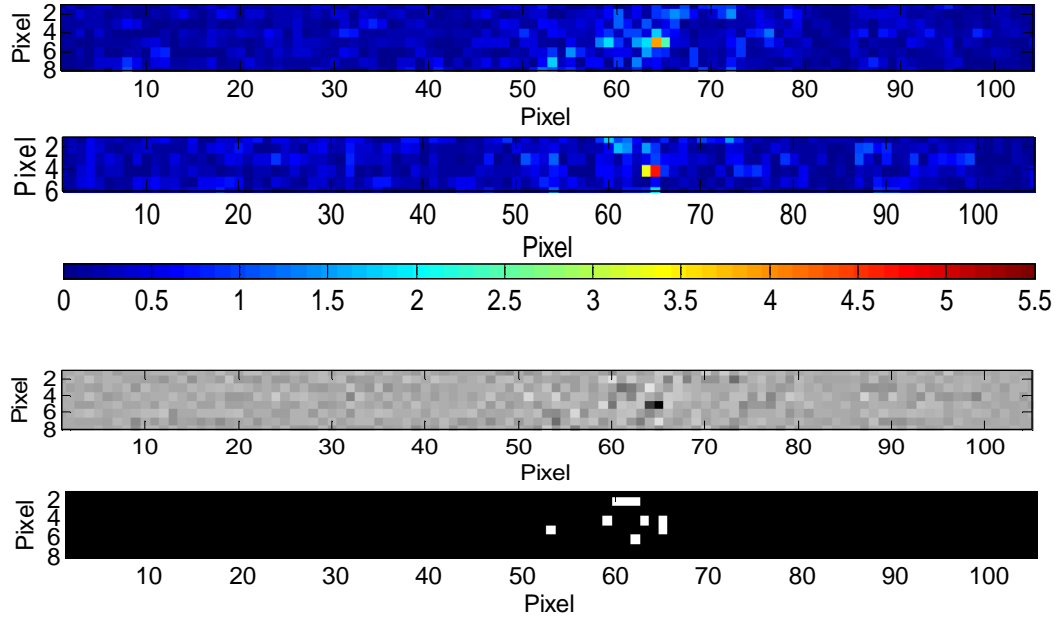


Figure 4.29. Heat column. (Top to bottom). Absolute second derivative in x direction and in y direction. Laplacian and Roberts filter.

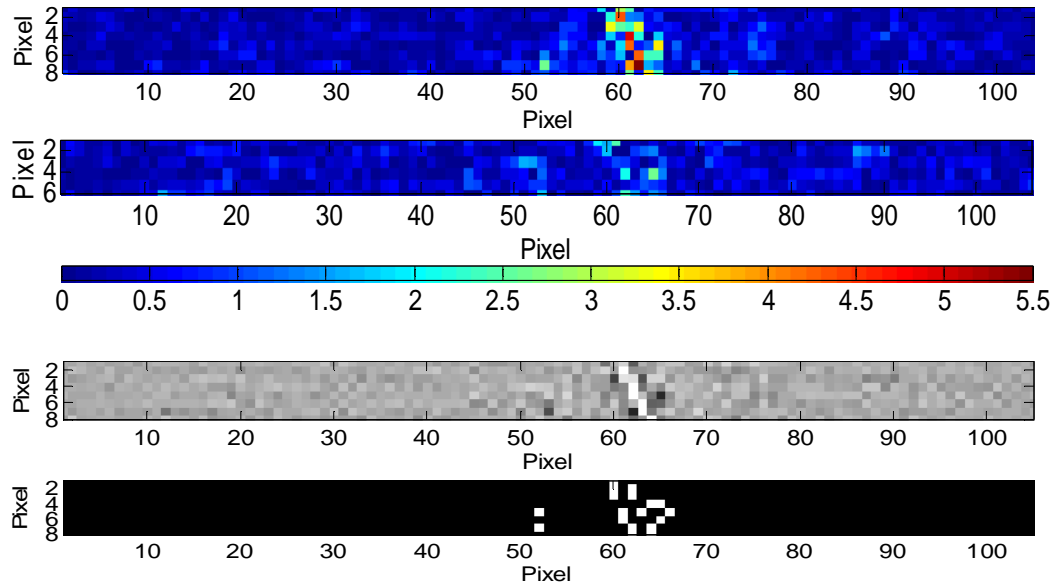


Figure 4.30. Crack. (Top to bottom). Absolute second derivative in x direction and in y direction. Laplacian and Roberts filter.

Computing the second derivatives, only the highest values of temperature changes are highlighted. Only the heat related to the failure evolution is pointed out; no features are showed in the bottom left part of the ROI. However, the results from the spatial filters could be clearer with the application of a smoothing filter. It could be helpful, in this study, to level the boundary of the warm region for a better visualization of the warm area.

Looking at more consequential frames, it is possible to appreciate the evolution of the heated region along the width of the gauge section and then to carry out conclusions about the state of damage of the area especially interested by the plastic deformation passing the time. As reported in literature [1], material dissipativity can be considered and used as a highly sensitive and accurate manifestation of damage. The physical process of degradation can be monitored by the infrared camera and

evaluated through the dimension of the heated area. Moreover, it is demonstrated above, that the correlation coefficient trend, computed in the first stage of the present algorithm, can add more information about the state of damage of the sample as it is related to the stress trend.

The lower is the coefficient, the higher is the damage.

Chapter 5

Conclusions and future works

We present in this chapter a discussion about the results obtained from the experiments thus far proposed and an initial study for a possible future development regarding an image processing algorithm suitable for other nondestructive testing techniques.

5.1 Discussion of the results

In the present work, we proposed an image processing algorithm for thermograms acquired during laser spot thermography and tensile test. The principal purpose of this study was the evaluation of the state of damage of the testing object in an automatic way. Infrared cameras are able to display the damaged areas but the observation of every single frame recorded requires a long time and an expert operator. We developed a two-stage algorithm able to flag automatically the presence of the defect through a quantitative analysis of the thermal data. Mathematics and statistical parameters departing from reference values regarding sound areas identified damage situations. In most of the experiments, it was possible to set a threshold for the correlation coefficient to separate baseline from damage scenarios. We obtained better results while inspecting the composite plates in correspondence of superficial induced cracks. The algorithm was not reliable at all in the case of impact related damage where several false positive identifications

occurred. In the second stage, only the frames marked as suspicious were analyzed with the aim of highlighting the defect signature. The computation of the spatial second derivative gave results more successful than the computation of the first derivative in concordance with the experiment reported in literature. However, for the bidirectional composite plate this qualitative analysis failed in the definition of the damage boundary. This was probably due to the preferential pattern for the heat propagation along the fiber directions that hides the distortion in the temperature distribution expected for the presence of the defect. Overall, the application of the Laplacian filter often outperformed the Roberts filter, although the latter seemed to better isolate the contour of the damaged area.

In conclusion, we can state that depending on the type of the defect and on the material tested, the algorithm gave more or less promising results. In general, the correlation coefficient was as a good indicator of the state of damage of the tested object and surprising results were obtained also in tensile testing where a relationship between the correlation trend and the stress trend as a function of the time was worked out.

More studies must be conducted in order to estimate the effective reliability of the presented image processing. Interest can be addressed to different materials, different types of damages and different nondestructive evaluation approaches.

5.2 Future developments

It could be interesting to develop algorithms for thermal image processing also in support of other nondestructive technique. Here is presented a primitive study for an algorithm suitable for infrared images from vibrothermography or thermosonics testing.

Vibrothermography and thermosonics NDT techniques entail the mapping of a structure's surface temperature while the structure is subjected to forced mechanical oscillations. Regions of imperfection convert energy to heat through viscoelastic dissipation, collision of internal free surfaces in cracks or other mechanisms. Discontinuities may appear hot when the surface temperature is mapped [1].

Considering this phenomenon, we decide to exploit the wavelet transformation, with the aim of extracting signal details representing the damaged areas. First, we describe briefly the modified algorithm based on the discrete wavelet transformation (DWT). The main purpose remains the automatic detection of defects, but some substantial changes with respect to the algorithm discussed previously are necessary. Then we provide an application of this algorithm to an infrared image characterized by some hot spots.

5.2.1 Overview about the discrete wavelet transformation

The discrete wavelet transformation (DWT) is a multi-resolution analysis technique that can be used to obtain the joint time-frequency information of a signal. When compared to traditional Fourier transforms that lose the time resolution of non-stationary signals, wavelet transforms retain both the time and the frequency

resolution. The wavelet transforms decompose the original signal by computing its correlation with a short-duration wave called the mother wavelet that is flexible in time and in frequency. Figure 5.1 presents the most common mother wavelet families.

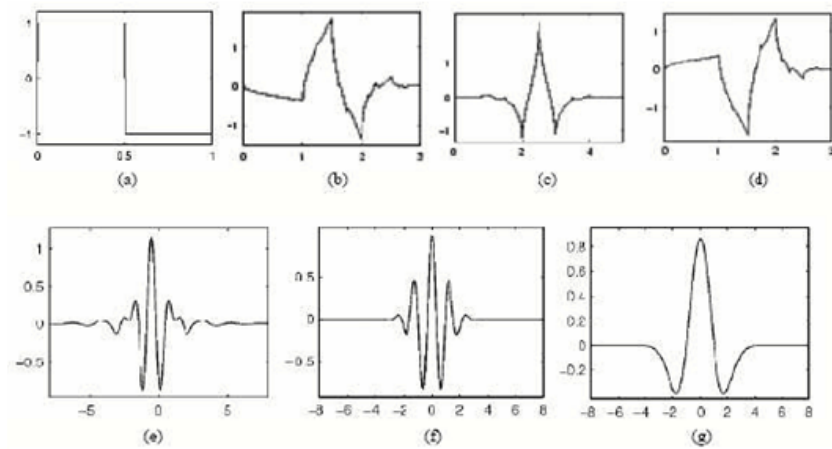


Figure 5.1. Wavelet families. (a) Haar. (b) Daubechies4. (c) Coiflet1. (d) Symlet2. (e) Meyer. (f) Morlet. (g) Mexican hat.

The DWT may be intuitively considered as a decomposition of a function (signal) following hierarchical steps (levels) of different resolutions (Figure 5.2a).

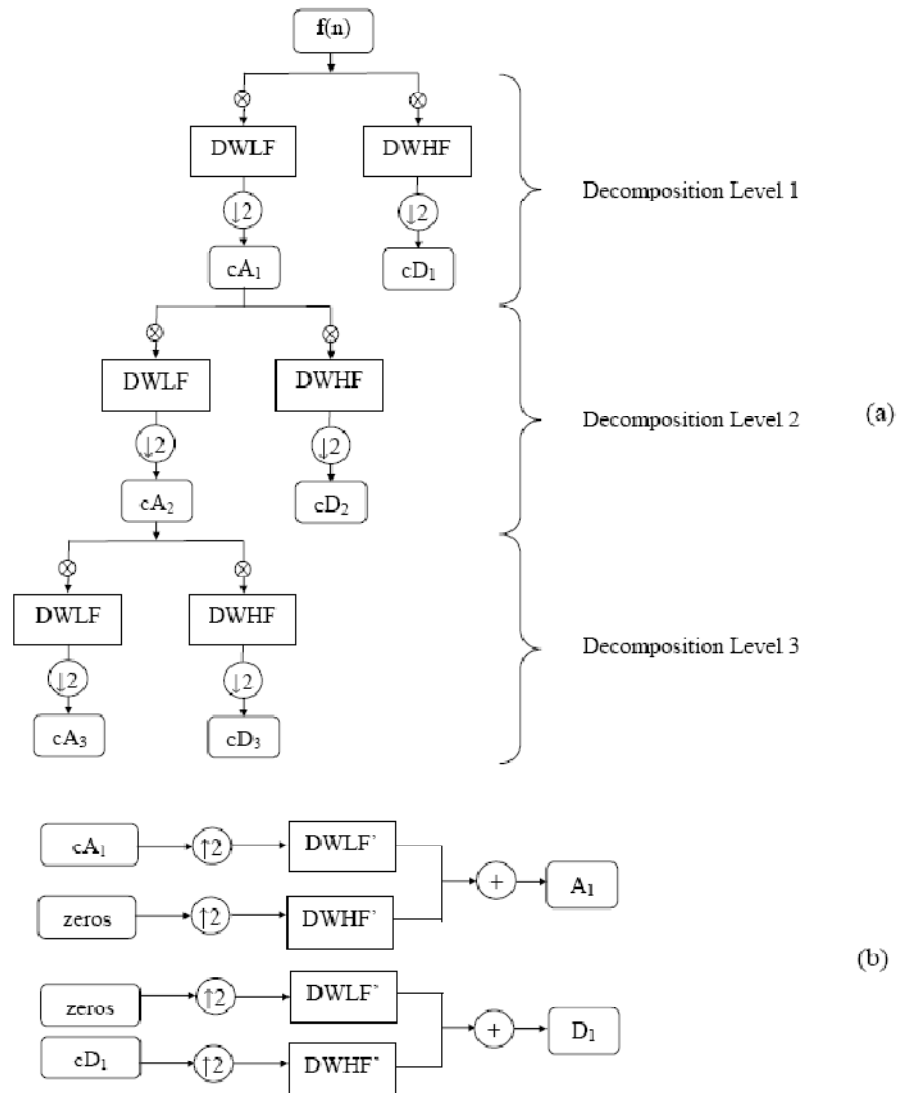


Figure 5.2. (a) Wavelet decomposition by filter bank tree; (b) signal reconstruction from wavelet coefficients; (c) reconstruction of original signal.

At the first step the function is decomposed into wavelet coefficients; low-frequency components (low-pass filtering) and high-frequency components (high-pass filtering) of the function are retained. The signal is therefore decomposed into separate frequency bands (scales). The filtering outputs are then downsampled. The number of wavelet coefficients for each branch is thus reduced by a factor of 2 such that the total number of points at a given level is that of the original signal. From the decomposed signal it is possible to extract only the feature desired. For example, de-noising and compression of the original signal can be achieved if only a few wavelet coefficients representative of the signal are retained and the remaining coefficients, related to noise, are discarded. The next step regards the process of reconstructing the time signal from the set of wavelet coefficients considered. Figure 5.2. (a) Wavelet decomposition by filter bank tree; (b) signal reconstruction from wavelet coefficients; (c) reconstruction of original signal. Figure 5.2b illustrates it. The coefficients are upsampled to regain their original number of points and then passed through a reconstruction lowpass filter, DWLF', and reconstruction highpass filter, DWHF'. Reconstruction by using the decomposition level α (scale 2^α), for example, is achieved by setting the wavelet coefficients from other scales equal to zero. Finally, the linear combination of the reconstructions from various decomposition levels results in the reconstruction of the original time signal [27].

5.2.2 Simulations for vibrothermography or thermosonics technique

The simulation proposed in this section regards the cutting out thermograph in Figure 5.3. Since the external stimulus starts to excite the tested object, the

discontinuities appears as hot spots and can be detect by computing the statistical parameters exploited in the previously presented experiment.

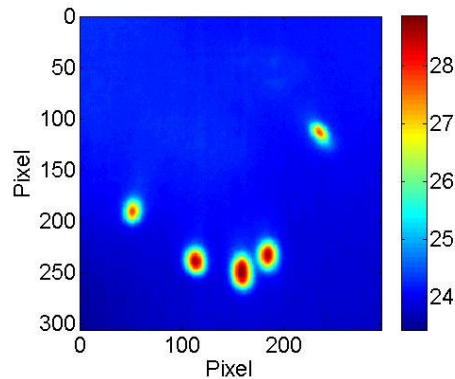


Figure 5.3. Third simulation. Hot spots in correspondence of the fingertips of a hand leaned behind a metal thin plate. The heat from the hand propagate for conduction into the plate and the hottest points are visualized by the infrared camera.

As soon as the external stimulus starts to excite the tested object, the discontinuities appears as hot signs and can be detect by computing the statistical parameters exploited in the experiments presented in the previous chapter. Eccentricity and correlation are not computed since warm tears rather than circles are expected. Because of the major familiarity with the wavelet applications for one-dimensional signals and for the easier understanding of this process, the analysis is conducted considering only one dimension. All the columns of the matrix (306 x 296) representing the thermograph above are stocked creating a vector of length 90576 elements. Figure 5.4 shows the linearization process and Figure 5.5 shows the application to the thermograph considered.

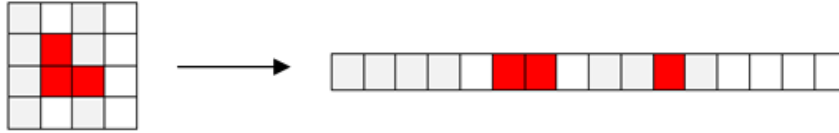


Figure 5.4. Linearization matrix to vector.

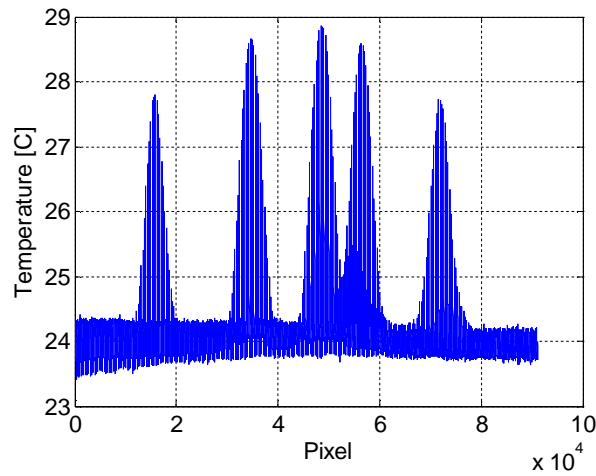


Figure 5.5. Third simulation. Linearization of the thermograph.

The oscillations in the signal are due to the linearization process as we verify noticing that the period corresponds to the length of the column of the original matrix. The five spikes that refer to the five hot spots are perfectly visible in Figure 5.3. The unidirectional signal is decomposed until the sixth level using the DWT based on a *sym8* mother wavelet since it presents similarities to the spike shape.



Figure 5.6. Sym8 mother wavelet.

Wavelet coefficients for the approximation and the six details are obtained through the Matlab function *wavedec*. Different threshold levels for each detail signals are set using the command *wdencmp* as follow:

$$**thr** = [0.5 1 1 1 1 0]$$

For each detail level only the wavelet coefficients higher than a value equal to the maximum coefficient multiplied for the threshold value are considered. In this particular case, the coefficients from the second to the forth level are neglected, all the coefficients of the fifth level are considered, and just the highest coefficients of the first detail level are kept (see vector *thr*). Figure 5.7 shows the reconstructed approximation and detail signals from these wavelet coefficients.

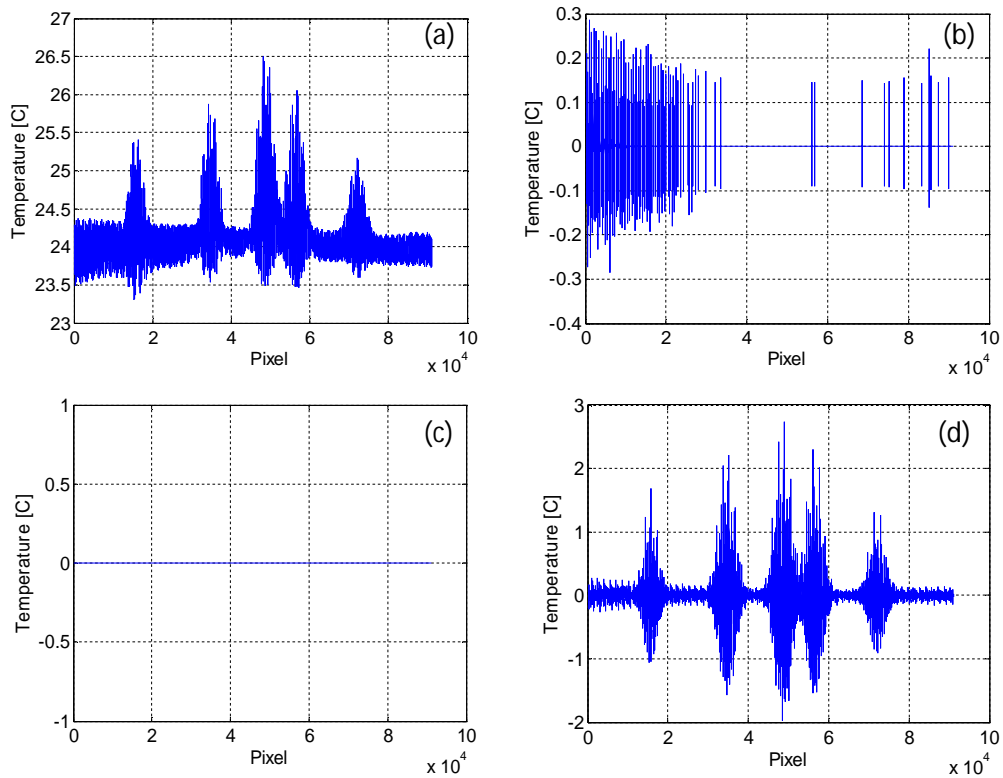


Figure 5.7. Third simulation. (a) Approximation signal. (b) Detail level 1. (c) Detail level 2. (d) Detail level 6.

The entire signal is reconstructed. Its mean and standard deviation are computed. Figure 5.8 marks all the values higher than three times the standard deviation of the recomposed signal.

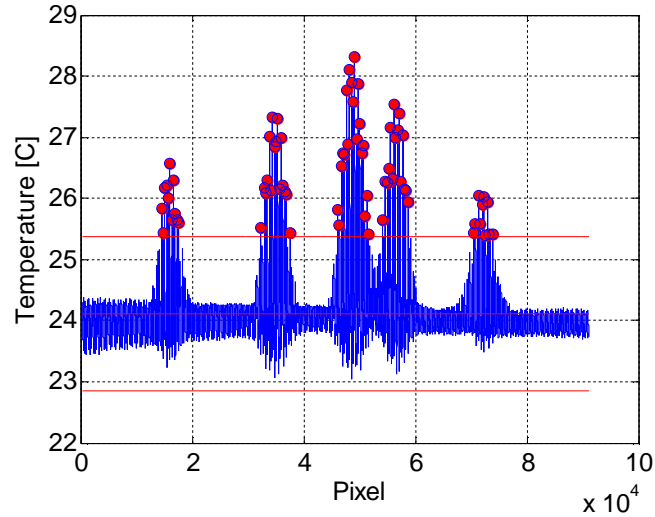


Figure 5.8. Third simulation. Reconstructed signal from the threshold levels. The red lines refer to the mean of the signal and the triple of standard deviation above and below it. The red spots mark the outlier values.

At this point plotting only the marked values the signal is reconvert into two dimensions. Figure 5.9 shows the result of the recomposition of the unidirectional processed signal.

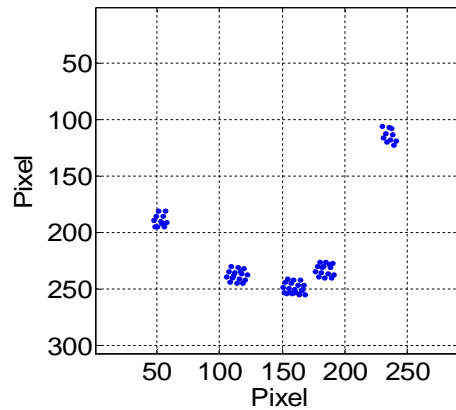


Figure 5.9. Third simulation. Map of the discontinuities.

It must be noticed that the hot spots of Figure 5.3 are well detected and mapped in Figure 5.9. Spatial filters and contrast adjustment can be helpful in highlighting the warmer features.

The results are promising since they show perfectly how this algorithm is able to detect the discontinuities into an image and then it can be hypothetically applied for damage detection in structural testing. Unfortunately, because of the lack of appropriate instrumentation for vibrothermography or thermosonics testing prevent us the chance to test this image processing algorithm onto real thermal images. This study can be a good starting point for a future development in the image processing in support of nondestructive evaluation techniques.

Figures caption

Figure 1.1. Schematization of the data acquisition setup for different stimulation techniques.

Figure 2.1. Classification of the electromagnetic radiations according to their wavelength and frequency.

Figure 2.2. Linear spatial filtering application.

Figure 2.3. Original image (a) and correspondent histogram (c). Enhanced image (b) and correspondent histogram (d).

Figure 2.4. Intensity functions in correspondence of two different types of edges and corresponding first derivatives.

Figure 2.5. Intensity function in correspondence of an edge and its first and second derivative.

Figure 3.1 First simulation. Six frames of the video sequence associated with no damage case.

Figure 3.2. First simulation. Last frames of the four video sequences that simulate the presence of damage. (a) Small 45° defect. (b) Large 45° defect. (c) Horizontal defect. (d) Vertical defect.

Figure 3.3. First simulation. (a) Correlation coefficient and (b) eccentricity associated with the frames of the five video sequences.

Figure 3.4. First simulation. Spatial derivative of the fifth frame of the sequence that simulate the presence of the large oblique crack. (a) First derivative along horizontal and vertical direction. (b) Second derivative along horizontal and vertical direction. (c) Absolute values of plots in (a). Absolute values of plots in (b).

Figure 3.5. First simulation. Results of the (a) Laplacian and (b) Roberts filter applied to the 13th frame of the sequence associated with the large oblique defect.

Figure 3.6. Second simulation. (a) Gaussian temperature distribution over a flat pristine surface. (b) Gaussian temperature distribution over the same surface having a vertical defect. (c) Simulated thermal image of (a). (d) Simulated thermal image of (b).

Figure 3.7. Second simulation. (a) First and second derivative along the horizontal axis for undamaged case. (b) First and second derivative along the vertical axis for undamaged case. (c) First and second derivative along the horizontal axis for the case with damage. (d) First and second derivative along the vertical axis for the case with damage.

- Figure 3.8.** Second simulation. Results of the (a) Laplacian and (b) Roberts filter applied to the “damaged” surface.
- Figure 4.1.** Experimental setup: marked horizontal guide, composite plate, laser source, infrared camera, cardboard box.
- Figure 4.2.** Schematization of the defects (blue color) and the scanning points (transparent circles) for the first experiment.
- Figure 4.3.** (a) Average temperature, (b) variance, (c) skewness, (d) kurtosis of the ROI of the video sequence associated with one of the pristine areas of the test specimen.
- Figure 4.4.** Thermal images of four scanned points. (a, b) Undamaged areas. (c, d) Damaged areas. All images had the highest kurtosis and skewness of their respective sequence.
- Figure 4.5.** (a) Correlation coefficient and (b) eccentricity associated with the 16 scanned points for the test object of the first experiment.
- Figure 4.6.** Absolute first derivative along x (leftmost column) and along y (second column). Absolute second derivative along x (third column) and along y (rightmost column). (a) Scanning point 10 (no damage). (b) Scanning point 11 (no damage). (c) Scanning point 2 (damage). (d) Scanning point 3 (damage).
- Figure 4.7.** Thermal image after the application of the Laplacian filter (left column) and Roberts filter (right column). (a) Scanning point 10 (no damage). (b) Scanning point 11 (no damage). (c) Scanning point 2 (damage). (d) Scanning point 3 (damage).
- Figure 4.8.** Schematization of the scanning points for the second experiment and zoom of the damaged area.
- Figure 4.9.** The problem of synchronization. Two consecutive frames of acquisition number 6 regarding a pristine area: (a) Frame 297 identified as first shot frame by skewness and kurtosis parameters; (b) Frame 298 identified as first shot frame by average temperature and variance parameters.
- Figure 4.10.** *First shot frame* for the recreated baseline video.
- Figure 4.11.** (a) Correlation coefficient and (b) eccentricity associated with the 37 scanned points for the test object of the second experiment.
- Figure 4.12.** Thermal images of four scanned points. (a, b) Undamaged areas. (c, d) Damaged areas. All images had the highest kurtosis and skewness of their respective sequence.
- Figure 4.13.** Absolute first derivative along x (leftmost column) and along y (second column). Absolute second derivative along x (third column) and along y (rightmost column). (a) Scanning point 5 (damage). (b) Scanning point 23 (damage).

Figure 4.14. Thermal image after the application of the Laplacian filter (left column) and Roberts filter (right column). (a) Scanning point 5(damage). (b) Scanning point 23 (damage).

Figure 4.15. Schematization of the defects and the scanning point positions for the third experiment.

Figure 4.16. (a) Correlation coefficient and (b) eccentricity associated with the 23 scanned points of the test object of the third experiment.

Figure 4.17. Thermal images of two scanned points. (a) Undamaged area (video sequence 21). (b) Damaged area (video sequence 8). All images had the highest kurtosis and skewness of their respective sequence.

Figure 4.18. Absolute first derivative along x (leftmost column) and along y (second column). Absolute second derivative along x (third column) and along y (rightmost column). (a) Scanning point 21(no damage). (b) Scanning point 8 (damage).

Figure 4.19. Thermal image after the application of the Laplacian filter (left column) and Roberts filter (right column). (a) Scanning point 21 (no damage). (b) Scanning point 8 (damage).

Figure 4.20. Production process (left) and microstructure scheme (right) for a DPS

Figure 4.21. The tensile coupon of high performance steel. The drawing of sample dimensions and the chemical composition.

Figure 4.22. Picture and schematization of the experimental setup: tensile testing machine, infrared camera, and connected control units.

Figure 4.23. Stress-strain curve (blue line) and stress trend as a function of time (red line).

Figure 4.24. (a) Average temperature, (b) variance, (c) skewness, (d) kurtosis of the ROI from the video sequence regarding a DPS sample .

Figure 4.25. Engineering stress trend (blue line) and correlation coefficient trend (red line) as a function of the time.

Figure 4.26. Four subdivisions for the correlation coefficient trend compared to four changes in the sample response to the displacement.

Figure 4.27. Temperature distribution on the sample surface at three different consequential instants. The colorbar indicates the temperature range [°C].

Figure 4.28. *Hot spot.* (Top to bottom). Absolute second derivative in x direction and in y direction. Laplacian and Roberts filter.

Figure 4.29. *Heat column.* (Top to bottom). Absolute second derivative in x direction and in y direction. Laplacian and Roberts filter.

Figure 4.30. *Crack.* (Top to bottom). Absolute second derivative in x direction and in y direction. Laplacian and Roberts filter.

Figure 5.1. Wavelet families. (a) Haar. (b) Daubechies4. (c) Coiflet1. (d) Symlet2. (e) Meyer. (f) Morlet. (g) Mexican hat.

Figure 5.2. (a) Wavelet decomposition by filter bank tree; (b) signal reconstruction from wavelet coefficients; (c) reconstruction of original signal.

Figure 5.3. Third simulation. Hot spots in correspondence of the fingertips of a hand leaned behind a metal thin plate. The heat from the hand propagate for conduction into the plate and the hottest points are visualized by the infrared camera.

Figure 5.4. Linearization matrix to vector.

Figure 5.5. Third simulation. Linearization of the thermograph.

Figure 5.6. Sym8 mother wavelet.

Figure 5.7. Third simulation. (a) Approximation signal. (b) Detail level 1. (c) Detail level 2. (d) Detail level 6.

Figure 5.8. Third simulation. Reconstructed signal from the threshold levels. The red lines refer to the mean of the signal and the triple of standard deviation above and below it. The red spots mark the outlier values.

Figure 5.9. Third simulation. Map of the discontinuities.

Tables caption

Table 2.1. Masks for edge detection

Table 4.1. Object parameters, setting instruction and unit of measurement

Table 4.2. Object parameters and acquisition features set for the first experiment

Table 4.3. Acquisition parameters for the second experiment

Table 4.4. Object and acquisition parameters for the second experiment

Acronyms

NDE	Nondestructive evaluation
NDT	Nondestructive testing
IR	Infrared
IRNDT	Infrared thermography for nondestructive testing
PIT	Passive infrared thermography
AIT	Active infrared thermography
DWT	Discrete wavelet transformation
ROI	Region of interest
CSV	Comma separated value
2D	Two dimensions
PC	Personal computer

Bibliography

- [1] X.P.V. Maldague, *Nondestructive testing handbook: Infrared and thermal testing*, 3rd ed. Columbus: American Society for Nondestructive testing, 2001.
- [2] Y.Y. Hung et al., "Review and comparison of shearography and active thermography for," *Materials Science and Engineering R*, pp. 75-112, 2009.
- [3] P.J. Shull, *Nondestructive Evaluation: theory, techniques, and applications*. New York: Marcel Dekker Ed., 2002.
- [4] U. Polimeno, M. Meo, D.P. Almond, and S.L. Angiolini, "Detecting Low Velocity Impact Damage in Composite Plate Using Nonlinear Acoustic/Ultrasound Methods," *Applied Composite Materials*, vol. 17, p. 418, 2010.
- [5] V.P Vavilov and D.A. Nesteruk, "Comparative Analysis of Optical and Ultrasonic Stimulation of Flaws in Composite Materials," *Russian Journal of Nondestructive Testing*, vol. 46, no. 2, p. 147, 2009.
- [6] A. Rashed, D.P. Almond, D.A. Rees, S. Burrows, and S. Dixon, "Crack Detection by Laser Spot Imaging Thermography," vol. 26, p. 500, 2007.
- [7] M. Morbidini, B. Kang, and P. Cawley, "Improved Reliability of Sonic Infrared Testing," *Materials Evaluation*, pp. 1193-02, 2009.
- [8] B. Weekes, P. Cawley, D.P. Almond, and T. Li, "The effect of crack opening on thermosonics and laser spot thermography," *Quantitative Nondestructive Evaluation*, vol. 29, p. 490, 2010.
- [9] G. Bolu, A. Gachagan, G. Pierce, G. Harvey, and L. Choong, "Monitoring Crack Propagation in Turbine Blades Caused by Thermosonics," *Review of Quantitative Nondestructive Evaluation*, vol. 29, pp. 1654-61, 2010.
- [10] J. M. Piau, A. H. Bendada, and X. Maldague, "Ultrasound Vibrothermography

- Applications for Nondestructive Discontinuity Detection," *Journal Materials Evaluation*, vol. 66, no. 10, pp. 1047-1052, 2008.
- [11] M. Morbidini and P. Cawley, "Reliable Crack Detection in Thermosonics NDE," *Review of Quantitative Nondestructive Evaluation* , vol. 27, 2008.
- [12] K. A. Tsoi and N. Rajic, "Interference Fit Fastener Inspection using Sonic Thermography," *Commonwealth of Australia* , 2007.
- [13] B. Kang and P. Cawley, "Low PZT Exciter for Thermosonics," *Review of Quantitative Nondestructive Evaluation*, vol. 26, pp. 484-91, 2007.
- [14] L. J. Pieczonca, W. J. Staszewski, F. Aymerich, and T. Uhl and M. Szewdo, "Numerical Simulation for Impact Damage Detection in Composites using Vibrothermography," *IOP Conf. Series: Material Science and Engineering 10* , 2010.
- [15] S. E. Burrows, A. Rashed, D. P. Almond, and S. Dixon, "Combined Laser Spot Imaging Thermography And Ultrasonic Measurements For Crack Detection," *Review of Quantitative Nondestructive Evaluation* , vol. 29, pp. 510–16, 2007.
- [16] T. Li, D. P. Almond, D. A. S. Rees, B. Weekes, and S. G. Pickering, "Pulsed Laser Spot Imaging Thermography, Modeling and Experimental Data," *Review of Quantitative Nondestructive Evaluation* , vol. 29, pp. 435–42, 2010.
- [17] Jeongguk Jim, "Tensile fracture characterization of thermosetting plastics by infrared thermography technique," *Key engineering materials*, vol. 417-418, pp. 433-436, 2010.
- [18] [Online]. <http://en.wikipedia.org/wiki/Infrared>].
- [19] C. Ibarra-Castaneda et al., "Infrared image processing and data analysis," *Elsevier B.V.*, vol. 46, pp. 75-83, 2004.
- [20] C. Gao and W. Q. Meeker, "A Statistical Method for Crack Detection from Vibrothermography Inspection Data," 2010.
- [21] M. Li, S. D. Holland, and W. Q. Meeker, "Automatic Crack Detection Algorithm for Vibrothermography Sequence-of-Images Data," *Review of Quantitative*

Nondestructive Evaluation, vol. 29, 2010.

- [22] R.C. Gonzales, R.E. Woods, and S.L.Eddins, *Digital Image Processing Using MATLAB*. New York, USA: Prentice-Hall, Inc. Upper Saddle River, 2003.
- [23] R.C. Gonzalez and R.E. Woods, *Digital Image Processing*. New York: Addison-Wesley Publishing Company, 1992.
- [24] T. Li, D.P. Almond, D.A.S. Rees, and B. Weekes, "Crack imaging by pulsed laser spot thermography," *Journal of Physics* , vol. Conference series 214, 2010.
- [25] FLIR System. (2010, March) User's manual FLIR 600 Series.
- [26] Marcello Vanali. (2010) Gruppo di misure termiche e meccaniche, Politecnico di Milano. [Online]. <http://misure.mecc.polimi.it/>
- [27] P. Rizzo and F Lanza di Scalea, "Wavelet-based Unsupervised and Supervised Learning Algorithms for Ultrasonic Structural Monitoring of Waveguides," in *Progress in Smart Materials and Structures Research.*: NOVA publishers, 2007, ch. 8, pp. 227-290.